



Self-luminous and Irradiated Exoplanetary Atmospheres Explored with HELIOS

Matej Malik^{1,2} , Daniel Kitzmann¹ , João M. Mendonça^{1,3} , Simon L. Grimm¹ , Gabriel-Dominique Marleau^{4,5}, Esther F. Linder⁴, Shang-Min Tsai^{1,6} , and Kevin Heng¹

¹ Center for Space and Habitability, University of Bern, Gesellschaftsstrasse 6, 3012, Bern, Switzerland; malik@umd.edu

² Department of Astronomy, University of Maryland, College Park, MD 20742, USA

³ Astrophysics and Atmospheric Physics, National Space Institute, Technical University of Denmark, Elektrovej, DK-2800 Kgs. Lyngby, Denmark

⁴ Physikalisch Institut, Universität Bern, Gesellschaftsstrasse 6, 3012 Bern, Switzerland

⁵ Institut für Astronomie und Astrophysik, Eberhard Karls Universität Tübingen, Auf der Morgenstelle 10, D-72076 Tübingen, Germany

⁶ Atmospheric, Oceanic, and Planetary Physics Department, Clarendon Laboratory, University of Oxford, Sherrington Road, Oxford OX1 3PU, UK

Received 2018 August 21; revised 2019 March 14; accepted 2019 March 15; published 2019 April 9

Abstract

We present new methodological features and physical ingredients included in the one-dimensional radiative transfer code HELIOS, improving the hemispheric two-stream formalism. We conduct a thorough intercomparison survey with several established forward models, including COOLTLUSTY and PHOENIX, and find satisfactory consistency with their results. Then, we explore the impact of (i) different groups of opacity sources, (ii) a stellar path length adjustment, and (iii) a scattering correction on self-consistently calculated atmospheric temperatures and planetary emission spectra. First, we observe that temperature–pressure (T – P) profiles are very sensitive to the opacities included, with metal oxides, hydrides, and alkali atoms (and ionized hydrogen) playing an important role in the absorption of shortwave radiation (in very hot surroundings). Moreover, if these species are sufficiently abundant, they are likely to induce nonmonotonic T – P profiles. Second, without the stellar path length adjustment, the incoming stellar flux is significantly underestimated for zenith angles above 80° , which somewhat affects the upper atmospheric temperatures and the planetary emission. Third, the scattering correction improves the accuracy of the computation of the reflected stellar light by $\sim 10\%$. We use HELIOS to calculate a grid of cloud-free atmospheres in radiative–convective equilibrium for self-luminous planets for a range of effective temperatures, surface gravities, metallicities, and C/O ratios to be used by planetary evolution studies. Furthermore, we calculate dayside temperatures and secondary eclipse spectra for a sample of exoplanets for varying chemistry and heat redistribution. These results may be used to make predictions on the feasibility of atmospheric characterizations with future observations.

Key words: methods: numerical – opacity – planets and satellites: atmospheres – radiative transfer – scattering

1. Introduction

With over 3500 confirmed exoplanet detections, we have a very large pool of objects at our fingertips waiting to be characterized. This abundance of potential data poses a challenge for numerical climate suites to deliver not only accurately but also within a reasonable time. At the core of the pyramid of atmospheric models sits the one-dimensional radiative transfer forward code, generating physically self-consistent atmospheric temperatures in radiative–convective equilibrium and mock planetary spectra. The one-dimensional format makes it ideally suited to include physics in colorful detail and be more flexible in applications than models of higher dimensions. Hence, it fulfills the role of the workhorse of exoplanetary atmospheric characterization. Although in past years, pure forward models have given some way to data-driven retrieval suites (e.g., Line et al. 2013; Lavie et al. 2017), which interpret data with the help of Bayesian statistics, forward models remain indispensable for providing accurate predictions for yet-to-be-assessed atmospheres. Even more, we are perhaps seeing a new dawn of self-consistent radiative transfer modeling, as it alone is able to provide the large training set of mock spectral data required by modern machine-learning algorithms (e.g., Márquez-Neila et al. 2018). Currently, there are several radiative transfer code families used in the exoplanetary field, with one branch of the ancestry originating from cool star studies and the other from planetary solar system modeling. The stellar branch is populated by the

SAM2 (Tsuji 1967, 1978, 2002) and PHOENIX (Allard & Hauschildt 1995; Hauschildt & Baron 1999) codes. The latter was also adapted for cooler exoplanets and brown dwarfs (Barman et al. 2005; Lothringer et al. 2018) but is still being used to model stellar atmospheres (Husser et al. 2013). A branch of this code, named DRIFT–PHOENIX, was extended by a consistently integrated cloud model (Helling et al. 2008). From a similar heritage comes COOLTLUSTY (Hubeny et al. 2003; Sudarsky et al. 2003), which is an offshoot of the stellar code TLUSTY (Hubeny 1988; Hubeny & Lanz 1995). The most prominent representative on the planetary side of the model tree is the Marley/Fortney code (Fortney et al. 2005, 2008), which was originally developed for solar system studies (McKay et al. 1989; Marley & McKay 1999) and modified for extrasolar applications (Marley et al. 1996). The DISORT codes (Stamnes et al. 1988; Meadows & Crisp 1996; Hamre et al. 2013) were inherited from the Earth sciences. In recent years, the codes ATMO (Amundsen et al. 2014), petitCODE (Mollière et al. 2015, 2017), GENESIS (Gandhi & Madhusudhan 2017), Exo–REM (Baudino et al. 2015), and HELIOS (Malik et al. 2017) emerged, written explicitly to treat exoplanetary conditions.

In this study, we build on HELIOS and present a number of improvements to its methodology. We compare the code in its updated form with other forward models and explore the importance of several physical and numerical radiative transfer ingredients.

In addition to the main purpose of this work, which is to present and discuss HELIOS’s updated form, we include two additional packages that may be of use to the community. First, we continue the legacy of past efforts to provide self-consistently calculated atmospheres of self-luminous young planets (Burrows et al. 1997; Chabrier et al. 2000; Baraffe et al. 2003, 2008; Mordasini et al. 2012), which often utilize precalculated atmospheric models, such as the BT-Settl grid (Allard et al. 2001, 2011; Allard 2014). The atmosphere, as the outermost boundary, determines the rate at which a young planet cools over time, gradually releasing its internal heat. Hence, it is imperative to connect the interior evolution model with the correct atmosphere to obtain an accurate description of the cooling process. The interior models and the atmospheres are calculated independently and stitched together at the radiative–convective boundary in the optically thick atmosphere or on top of the outermost layer of the convective interior model. The entropy, providing the connection to the formation process (Marleau & Cumming 2014), in this zone determines which two models fit together. To this end, grids of atmospheres are calculated that commonly span a parameter space in effective temperature, surface gravity, and metallicity. In addition to the entropy value at the lower atmospheric boundary, the other important output of atmospheric models is the emission spectrum, which helps assess the planet’s observability at various stages during its evolution and gives information on the formation history (Spiegel & Burrows 2012).

Even though many precalculated model grids exist, continuous progress is being made regarding opacity and chemical data. We hope that our completely new, alternative atmosphere grid may be of use to the community.

Furthermore, we use our modeling machinery to provide the community with self-consistently calculated cloud-free atmospheres for a variety of irradiated planets of current interest, including super-Earths, sub-Neptunes, hot Jupiters, and ultra-hot Jupiters. Using various C/O ratios, metallicities, and heat redistribution efficiencies, we generate a suite of predictive models for the dayside temperatures and secondary eclipse spectra for the planets explored.

All of our numerical codes used in this work are open-source and publicly available at github.com/exoclime.

2. New Features of HELIOS

In the year since its first appearance in Malik et al. (2017), HELIOS has undergone a number of methodological improvements. In this section, we elucidate the main new features and sketch out the corresponding algebra and core equations. As an overview, HELIOS now includes the following features.

1. A direct irradiation beam decouples the stellar flux from atmospheric thermal emission. It allows us to model an atmospheric column at a specific latitude and longitude, whereas before, one was restricted to average hemispheric or global conditions.
2. Convective adjustment may be applied to correct atmospheric layers that are convectively unstable. Convection is expected to take over as the main energy transport mechanism in the deep atmospheric layers.
3. The contribution function for each wavelength bin is now available as output. This makes it possible to identify the wavelength-dependent photosphere.

4. A geometrical correction to the stellar beam path length is included, which proves important for large zenith angles. Without this correction, the attenuation of the stellar irradiation is overestimated in plane-parallel grids.
5. We add a correction factor to the two-stream equations that improves the accuracy of the scattered flux in the hemispheric two-stream prescription.
6. We employ a vastly expanded list of opacity of sources, including an ample mixture of infrared absorbers, metal and other hydrides, metal oxides, the alkali metals Na and K, and H⁻.

We now discuss each improvement in turn.

2.1. Direct Irradiation Beam

2.1.1. Definitions

In HELIOS’s original design, the stellar shortwave flux and planetary thermal flux were treated equally using the two-stream approximation (Malik et al. 2017). With only the two-stream fluxes, it is not possible to set a stellar irradiation angle. Furthermore, the temperatures on the planetary dayside can only be adjusted *globally* by the *f* heat redistribution parameter, which sets the efficiency of heat exchange between the day- and nightside of the planet (Spiegel & Burrows 2010). However, it is not possible to model the local radiative balance for a given latitude and longitude. We account for these two insufficiencies by extending the two-stream equations to incorporate a direct stellar beam in addition to the two-stream flux expressions. This separation of stellar flux and planetary emission has been well known in the planetary science literature (Toon et al. 1989); however, in contrast to earlier studies, we do not differentiate between shortwave and longwave radiation. Our flux expressions hold irrespective of the explored wavelength.

In the following, we define the relevant physical quantities, which deviate slightly from the definitions given in Heng et al. (2018). Nonetheless, the subsequent derivations and final flux expressions are identical.

Let us start with the plane-parallel radiative transfer equation,

$$\mu \frac{dI^{\text{tot}}}{d\tau} = I^{\text{tot}} - S, \quad (1)$$

which provides the change of the total intensity I^{tot} with optical depth τ . The intensity generally depends on the zenith and azimuth angles θ and ϕ , while τ simply measures the vertical change in optical depth, increasing in the downward direction. By convention, θ is measured from the upward-pointing plane normal vector, which makes $\mu = \cos \theta$ negative for downward-pointed and positive for upward-pointed radiation rays. The function S incorporates all radiation sources that add to the intensity I^{tot} . It is written as (Chandrasekhar 1960; Mihalas 1970, 1978)

$$S = (1 - \omega_0)B + \frac{\omega_0}{4\pi} \int_0^{4\pi} \mathcal{P}(\theta, \phi; \theta', \phi') I^{\text{tot}}(\theta', \phi') d\Omega', \quad (2)$$

where the first term is the thermal blackbody emission with the Planck function B and the single-scattering albedo ω_0 . The latter describes the relative strength of atmospheric extinction

due to scattering only to the total extinction, which is scattering and absorption. The second term considers the incoming rays from the direction (θ', ϕ') and calculates, by multiplying them with the scattering phase function \mathcal{P} , whether they are scattered into the line of sight (θ, ϕ) . The integral over all possible incoming angles provides the total addition of scattered intensity to the source function S .

In addition to our previous theoretical excursion in Malik et al. (2017), here we divide the total intensity

$$I^{\text{tot}} = I^{\text{dir}} + I^{\text{diff}} \quad (3)$$

into the direct stellar beam I^{dir} and the diffuse intensity I^{diff} ⁷. The direct beam changes with the optical depth as

$$I^{\text{dir}} = F_{*,\text{TOA}} e^{\tau/\mu} \delta(\mu - \mu_*) \delta(\phi - \phi_*), \quad (4)$$

propagating on a straight line through the atmosphere downward along the stellar angles $\theta_* = \cos^{-1} \mu_*$ and ϕ_* .

The incoming stellar flux at the top of the atmosphere (TOA) is given by

$$F_{*,\text{TOA}} = \left(\frac{R_*}{a} \right)^2 F_*, \quad (5)$$

where R_* is the stellar radius, a is the orbital distance, and F_* is the stellar surface flux, which can be approximated by either the blackbody Planck function B for the stellar temperature T_* , i.e., $F_* = \pi B(T_*)$, or a synthetic model spectrum, e.g., PHOENIX (Husser et al. 2013) or Kurucz/ATLAS (Kurucz 1979; Murphy & Meiksin 2004; Munari et al. 2005). The flux associated with the direct beam is

$$\begin{aligned} F^{\text{dir}} &\equiv - \int_0^{2\pi} \int_{-1}^1 \mu I^{\text{dir}} d\mu d\phi, \\ &= -\mu_* F_{*,\text{TOA}} e^{\tau/\mu_*}, \end{aligned} \quad (6)$$

also simultaneously leading to the upper boundary condition of $F_{\text{TOA},\downarrow} = -\mu_* F_{*,\text{TOA}}$, where $\tau = 0$. The leading minus sign in Equation (6) is needed because we define the radiative flux to always be a positive quantity.

The diffuse up- and downward fluxes are defined as

$$\begin{aligned} F_{\uparrow}^{\text{diff}} &\equiv \int_0^{2\pi} \int_0^1 \mu I^{\text{diff}} d\mu d\phi, \\ F_{\downarrow}^{\text{diff}} &\equiv - \int_0^{2\pi} \int_{-1}^0 \mu I^{\text{diff}} d\mu d\phi, \end{aligned} \quad (7)$$

from which we immediately obtain the total up- and downward fluxes, $F_{\uparrow} = F_{\uparrow}^{\text{diff}}$ and $F_{\downarrow} = F_{\downarrow}^{\text{diff}} + F^{\text{dir}}$. Note that the planetary thermal emission is included in the diffuse component of the flux.

2.1.2. Interface Flux Expressions

For the in-depth derivation of the diffuse fluxes, we refer the reader to Heng et al. (2018). Here we specifically present and write the diffuse flux expressions as included in HELIOS. From here on, we omit the superscript “diff” and subscript i for certain quantities, e.g., ω_0 , for better readability. The fluxes at the i th interface in the staggered numerical grid (see Malik et al.

2017, Figure 2) read

$$\begin{aligned} F_{i,\uparrow} &= \frac{1}{\chi} \left(\psi F_{i-1,\uparrow} - \xi F_{i,\downarrow} + 2\pi\epsilon \mathcal{B}_{\uparrow} + \frac{1}{\mu_*} \mathcal{I}_{\uparrow} \right), \\ F_{i,\downarrow} &= \frac{1}{\chi} \left(\psi F_{i+1,\downarrow} - \xi F_{i,\uparrow} + 2\pi\epsilon \mathcal{B}_{\downarrow} + \frac{1}{\mu_*} \mathcal{I}_{\downarrow} \right), \end{aligned} \quad (8)$$

where

$$\begin{aligned} \mathcal{B}_{\uparrow} &\equiv (\chi + \xi) B_i - \xi B_{i-1} + \frac{\epsilon}{1 - \omega_0 g_0} (\chi - \xi - \psi) B', \\ \mathcal{I}_{\uparrow} &\equiv \psi \mathcal{G}_{+} F_{i-1}^{\text{dir}} - (\xi \mathcal{G}_{-} + \chi \mathcal{G}_{+}) F_i^{\text{dir}}, \\ \mathcal{B}_{\downarrow} &\equiv (\chi + \xi) B_i - \psi B_{i+1} + \frac{\epsilon}{1 - \omega_0 g_0} (\xi - \chi + \psi) B', \\ \mathcal{I}_{\downarrow} &\equiv \psi \mathcal{G}_{-} F_{i+1}^{\text{dir}} - (\chi \mathcal{G}_{-} + \xi \mathcal{G}_{+}) F_i^{\text{dir}}, \end{aligned} \quad (9)$$

and $B_i = B(T_i)$ is the Planck function evaluated for the temperature at interface i . Further, we use above

$$\begin{aligned} \chi &\equiv \zeta_-^2 T^2 - \zeta_+^2, \\ \xi &\equiv \zeta_+ \zeta_- (1 - T^2), \\ \psi &\equiv (\zeta_-^2 - \zeta_+^2) T, \\ \zeta_{\pm} &\equiv \frac{1}{2} \left[1 \pm \left(\frac{1 - \omega_0}{1 - \omega_0 g_0} \right)^{1/2} \right], \\ \mathcal{G}_{\pm} &\equiv \frac{1}{2} \left[\mathcal{L} \left(\frac{1}{\epsilon} \pm \frac{1}{\mu_* (1 - \omega_0 g_0)} \right) \pm \frac{\omega_0 g_0 \mu_*}{1 - \omega_0 g_0} \right], \\ \mathcal{L} &\equiv \frac{(1 - \omega_0)(1 - \omega_0 g_0) - 1}{1/\mu_*^2 - 1/\epsilon^2 (1 - \omega_0)(1 - \omega_0 g_0)}, \\ B' &\equiv \frac{\Delta B}{\Delta \tau}, \end{aligned} \quad (10)$$

where the last equation in Equation (10) shows our choice of expanding the Planck function linearly in optical depth, with ΔX representing the difference of any quantity X across a layer. Setting $B' = 0$ and $B_{i\pm 1} \rightarrow B_i$ in Equation (9) translates into a model with isothermal layers. Equation (8) is valid for nonisotropic coherent scattering with the direction of scattering given by the asymmetry parameter $g_0 \in [-1, 1]$, as defined in, e.g., Goody & Yung (1989) or Pierrehumbert (2010). The transmission function is given as

$$T \equiv e^{-1/\epsilon \sqrt{(1 - \omega_0 g_0)(1 - \omega_0)}} \Delta \tau. \quad (11)$$

We make use of the first Eddington coefficient ϵ , which is defined as the assumed (constant) ratio between the first and second moments of the intensity and is the inverse of the commonly known diffusivity parameter \mathcal{D} (Armstrong 1968; Heng et al. 2014). The latter effectively determines how diffuse the radiation behaves ($\mathcal{D} = 2$: fully isotropic radiation; $\mathcal{D} = 1$: fully vertically oriented radiation).

⁷ We use the label *diffuse* for radiation that has been either scattered or emitted by the planetary atmosphere.

In the case of $\omega_0 = 1$ (pure scattering), Equation (8) needs to be replaced by

$$\begin{aligned} F_{i,\uparrow} &= F_{i-1,\uparrow} + \frac{(F_{i,\downarrow} - F_{i-1,\uparrow})(1 - g_0)\Delta\tau}{(1 - g_0)\Delta\tau + 2\epsilon} + \mathcal{J}_{\uparrow}, \\ F_{i,\downarrow} &= F_{i+1,\downarrow} + \frac{(F_{i,\uparrow} - F_{i+1,\downarrow})(1 - g_0)\Delta\tau}{(1 - g_0)\Delta\tau + 2\epsilon} + \mathcal{J}_{\downarrow}, \end{aligned} \quad (12)$$

where

$$\begin{aligned} \mathcal{J}_{\uparrow} &\equiv \frac{1}{(1 - g_0)\Delta\tau + 2\epsilon} \mathcal{K}_{\uparrow}, \\ \mathcal{K}_{\uparrow} &\equiv [\mu_* + (1 - g_0)\Delta\tau + \epsilon] F_i^{\text{dir}} - (\mu_* + \epsilon) F_{i-1}^{\text{dir}}, \\ \mathcal{J}_{\downarrow} &\equiv \frac{1}{(1 - g_0)\Delta\tau + 2\epsilon} \mathcal{K}_{\downarrow}, \\ \mathcal{K}_{\downarrow} &\equiv [\mu_* - (1 - g_0)\Delta\tau - \epsilon] F_i^{\text{dir}} - (\mu_* - \epsilon) F_{i+1}^{\text{dir}}. \end{aligned} \quad (13)$$

Although in real atmospheres, the limit $\omega_0 = 1$ is strictly academic, we include those expressions in the code for numerical stability reasons when $\omega_0 > 1 - |\epsilon|$, with $|\epsilon| \ll 1$.

2.2. Convective Adjustment

We account for atmospheric convection by adjusting the superadiabatic lapse rates back to the dry adiabatic lapse rate (Manabe et al. 1965; Manabe & Wetherald 1967). In the model grid, we check for each pair of adjacent layers i and $i + 1$ (the latter being above the former) whether

$$T_{i+1} \geq T_i \left(\frac{P_{i+1}}{P_i} \right)^{\kappa} \quad (14)$$

is satisfied, where T is the temperature, P is the pressure, and κ is the adiabatic coefficient, for which we use the definition from the planetary climate literature

$$\kappa \equiv \left(\frac{d \ln T}{d \ln P} \right)_S, \quad (15)$$

with S being the entropy. In stellar astrophysics, κ corresponds to $\nabla_{\text{ad}} \equiv (\Gamma_2 - 1)/\Gamma_2$ with

$$\Gamma_2 \equiv \left[1 - \frac{P}{c_P \rho T} \frac{\chi_T}{\chi_\rho} \right]^{-1}, \quad (16)$$

where c_P is the specific heat capacity, ρ is the density, $\chi_T \equiv (\partial \ln P / \partial \ln T)_\rho$, and $\chi_\rho \equiv (\partial \ln P / \partial \ln \rho)_T$ (Hansen et al. 2004). Invoking Equation (14) is equivalent to testing for Schwarzschild's criterion. If the condition is not satisfied, we correct the temperatures back to the adiabatic lapse rate.

To find the correct adiabat in the convective region, we check for one additional criterion. As convection does not create or eliminate energy, we demand that the enthalpy, which is the total internal energy plus the work done to reach equilibrium with the surrounding medium, must be conserved within a convective region. In our one-dimensional case, the quantity of interest is the product of the specific enthalpy, i.e., enthalpy per unit mass, and m_{col} is the column mass,

$$\int_{\text{conv.region}} \widetilde{H} dm_{\text{col}} = \int_{\text{conv.region}} \widetilde{H}' dm_{\text{col}}, \quad (17)$$

where we evaluate the integral over the whole convective region. The prime superscript denotes a quantity after the adjustment. From thermodynamics and the ideal gas law,

$$dH = dU + d(PV) = C_V dT + nRdT, \quad (18)$$

with the volume V ; the heat capacities at constant volume and pressure, C_V and C_P , respectively; and the number of gas particles N . With $C_V + nR = C_P$, we obtain $dH = C_PdT$. Integrating, dividing by mass, and inserting into Equation (17) leads to

$$\int_{\text{conv.region}} c_P T dP = \int_{\text{conv.region}} c'_P T' dP, \quad (19)$$

with c_P being the specific heat capacity per unit mass. We have further substituted $m_{\text{col}} = P/g$ and used the common assumption of treating g as constant throughout the atmosphere. As the solution T' is following an adiabat, it is convenient to express it via the potential temperature Θ , which is constant along the adiabat, so that

$$T'(P) = \Theta \left(\frac{P_0}{P} \right)^{-\kappa}, \quad (20)$$

where we denote P_0 as a reference pressure (e.g., the bottom of the convective region). The potential temperature satisfying Equation (17) is

$$\Theta = \frac{\int_{\text{bot}}^{\text{top}} c_P T dP}{\int_{\text{bot}}^{\text{top}} c_P (P_0/P)^{-\kappa} dP}, \quad (21)$$

where “top” and “bot” mark the top and bottom boundaries of the convective region (Mendonça et al. 2018b).

Numerically, it is necessary to iterate between radiative convergence and convective adjustment. In practice, the following procedure is executed.

1. HELIOS iterates until the atmosphere is in radiative equilibrium. See Malik et al. (2017) for more details.
2. All layers are checked for unstable lapse rates with Equation (14).
3. If unstable layers are found, they are corrected as described by Equations (20) and (21).
4. Pairs of layers whose in-between lapse rate has been corrected are now called convective layers.
5. One forward step with the radiative iteration is executed. Since this again changes the lapse rates, steps 2–4 need to be repeated.
6. In general, steps 2–5 are repeated until a converged solution is found. Such a solution needs to satisfy (i) convective stability, (ii) local radiative equilibrium in all radiative layers, and (iii) global energy equilibrium. Whereas criteria (i) and (ii) are inherent to the convective adjustment mechanism, the satisfaction of the global energy criterion is somewhat more tricky. We discuss our method of how to solve it in Appendix D.

The net convective flux, which is nonzero in the convective layers, is a by-product of the convective adjustment and reads $\mathcal{F}_{\text{conv},-} = \mathcal{F}_- - \mathcal{F}_{\text{rad},-}$, where \mathcal{F}_- is the net flux and $\mathcal{F}_{\text{rad},-}$ is the net radiative flux. We denote a wavelength-independent flux by \mathcal{F} .

In this work, we employ the equation of state of Saumon et al. (1995) to obtain the adiabatic coefficient. A simple ideal

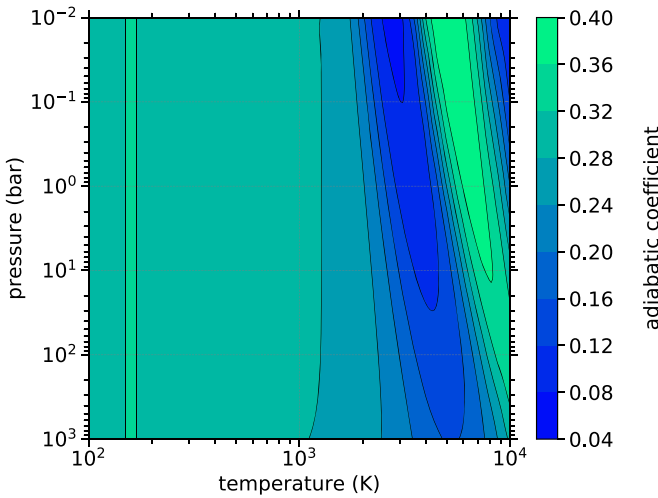


Figure 1. Adiabatic coefficient vs. temperature and pressure for lower atmospheres. The black contour lines are separated by 0.04. The values depicted are for solar metallicity and carbon-to-oxygen ratio.

gas extension toward lower pressures ($P < 10^{-2}$ bar) and temperatures ($T \lesssim 100$ K) was included by Alibert et al. (2005) and Mordasini et al. (2012). Since the species other than hydrogen and helium (the metals) represent a small contribution by mass, we include them only approximately in the calculation of the adiabatic gradient. As in Baraffe et al. (2008), we compute the effective helium fraction $Y_{\text{eff}} = Y + Z$, with $X + Y + Z = X + Y_{\text{eff}} \equiv 1$, where X , Y , and Z are the mass fractions of elemental hydrogen, helium, and the metal elements. We then use Y_{eff} to interpolate within the Saumon et al. (1995) tables.

Figure 1 shows κ in the temperature–pressure (T – P) regime of interest. The low values of $\kappa \sim 0.04$ around 3000 K come from the dissociation of molecular hydrogen, and those near 10⁴ K come from the ionization of atomic hydrogen.

To obtain the heat capacity, we use Equation (2.11) in Pierrehumbert (2010), $c_P = k_B/(\mu m_u \kappa)$, with the Boltzmann constant k_B , the mean molecular weight μ , and the atomic mass unit m_u . In the last stages of this work, we realized that this expression is valid only in the limit of a perfect gas (i.e., with a constant number of degrees of freedom) or when the number of degrees of freedom changes independently of pressure. Since this is not given at dissociation or ionization of hydrogen, for instance, the heat capacity turns out to be underestimated by a factor of ~ 3 in those narrow temperature regions. Explicitly, one can show easily (see Appendix E) that the correct equation is

$$c_P = \frac{k_B}{m_u \kappa} \left(-\frac{\partial \tilde{S}}{\partial \ln P} \right)_T, \quad (22)$$

where $\tilde{S} \equiv S/(k_B/m_u)$ is dimensionless. As the Sackur-Tetrode equation reveals and we verified numerically, the point is that the factor $(-\partial \tilde{S}/\partial \ln P)_T$ is equal to $1/\mu$ everywhere in the perfect gas portion of the T – P plane, recovering the limit of Pierrehumbert (2010), except where, for instance, the dissociation and ionization of hydrogen and, to a lesser extent, the ionization of helium or metals occur. For our models, we verified that changing c_P does not lead to any noticeable differences in the obtained T – P profile (not shown).

2.3. The Contribution Function

Another addition to HELIOS is the output of the contribution function and the transmission weighting function. They both serve the purpose of finding the photosphere with and without consideration of the atmospheric emission, respectively. Considering a simple two-stream model with isothermal layers and pure absorption, the upward flux at the i th interface reads

$$F_{i,\uparrow} = T_{i-1} F_{i-1,\uparrow} + 2\pi\epsilon B_{i-1}(1 - T_{i-1}). \quad (23)$$

Being interested in the TOA flux, we set the index i in the previous expression to the TOA and take all layers below into account. This leads to

$$F_{\text{TOA},\uparrow} = F_{\text{BOA},\uparrow} \prod_{i=0}^{n-1} T_i + \sum_{i=0}^{n-1} \left[2\pi\epsilon B_i(1 - T_i) \prod_{j=i+1}^{n-1} T_j \right], \quad (24)$$

with n being the number of layers. Using the altitude z as the vertical grid coordinate, Equation (24) is equivalent to

$$F_{\text{TOA}} = F_{\text{BOA}} T(z_{\text{BOA}}, z_{\text{TOA}}) + \int_{z_{\text{BOA}}}^{z_{\text{TOA}}} B(z) \frac{d\mathcal{T}(z, z_{\text{TOA}})}{dz} dz, \quad (25)$$

where $\mathcal{T}(z, z_{\text{TOA}})$ is the total transmission between the atmosphere at altitude z and TOA. In a discrete layer model, the integral term directly translates to the bracket term in Equation (24). This term represents the contribution of a specific layer i to the TOA spectral emission, hence the name *contribution function* (Irwin 2009). Physically, it corresponds to the atmospheric location where the transmission function \mathcal{T} exhibits the steepest gradient, weighted by the layer’s emission. Without the consideration of the emission, one obtains the *transmission weighting function* Ψ , which simply reads

$$\Psi_i = (1 - T_i) \prod_{j=i+1}^{n-2} T_j. \quad (26)$$

Usually, the contribution function is the quantity analyzed to determine the origin of the planetary emission for a given wavelength. The according atmospheric layer is given by the location, where the contribution function peaks.

2.4. Stellar Path Length Correction

In the plane-parallel assumption, the stellar photons are assumed to travel along a straight path, which manifests itself in the use of a constant stellar zenith angle θ_* throughout the model grid. However, for large zenith angles,⁸ the stellar beam path length, proportional to $1/\cos(\theta_*)$, is substantially overestimated; i.e., the path length exceeds the real atmospheric extent. If taking the spherical geometry into account, the stellar path length needs to be corrected downward. This is done by adjusting the zenith angle θ_* and, consequently, $\mu_* = \cos(\theta_*)$,

⁸ Here and in the rest of this work, we deviate from our definition of θ_* in Section 2.1.1 and scan the range from 0° to 90° with the zenith angle when going from the substellar point to the limb of the planet. In this sense, a large zenith angle corresponds to planetary limb regions.

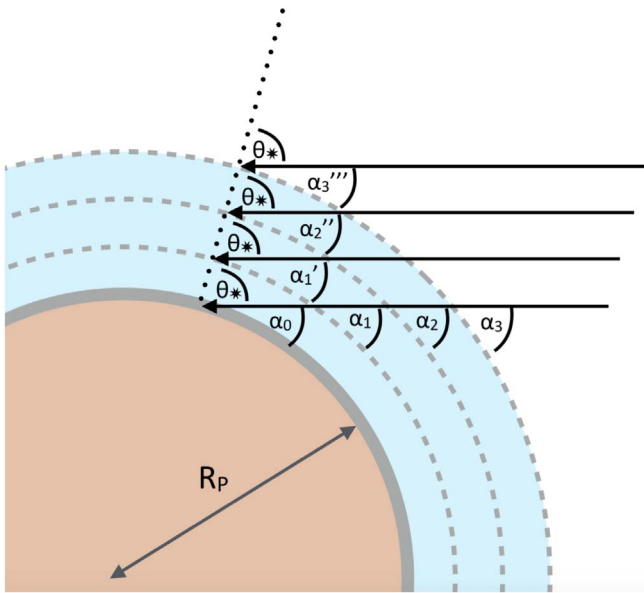


Figure 2. Applying a vertical column model (located at the dotted line) to spherical geometry requires a correction of the stellar zenith angle θ_* , depending on the location in the atmosphere. First, the zenith angle decreases with altitude. In terms of $\alpha_0 = 90^\circ - \theta_*$, this means that $\alpha_0 < \alpha_1 < \alpha_2 < \alpha_3$ for layers 0 to 3. Second, each model layer is reached by stellar photons that have traveled along a different path (solid lines), such that $\alpha_1 \neq \alpha'_1$, $\alpha_2 \neq \alpha'_2$, $\alpha_3 \neq \alpha'_3$, etc.

depending on the location in the atmosphere. In Figure 2, the situation is drawn for a vertical column model with three layers, located along the dotted line. First, the zenith angle should depend on the altitude, which means that $\alpha_0 < \alpha_1 < \alpha_2 < \alpha_3$ in Figure 2 for $\alpha_0 = 90^\circ - \theta_*$. Second, each layer of the model is reached by stellar photons that traveled along a different path through the planetary hemisphere, i.e., $\alpha_1 \neq \alpha'_1$, $\alpha_2 \neq \alpha'_2$, $\alpha_3 \neq \alpha'_3$, etc. We rewrite and implement Li & Shibata's (2006) Equation (2) as

$$\mu_{*,ij} = -\sqrt{1 - \left(\frac{R_{\text{pl}} + z_i}{R_{\text{pl}} + z_j}\right)^2(1 - \mu_*)} \quad \forall j \geq i, \quad (27)$$

where z is the altitude and R_{pl} is the planetary radius. For each layer i , one must consider the stellar pathway through all overlying layers j separately with $\mu_{*,ij}$ (see the Appendix in Mendonça et al. 2018a). We set R_{pl} as the planet's measured white-light radius and associate it with a pressure of 10 bars (as done, e.g., in Kreidberg et al. 2015).⁹ The height difference from layer j to R_{pl} is given by z_j (and, analogously, for layer i). The quantity μ_* corresponds to the stellar zenith angle at the layer of interest i . As expected, $\mu_{*,ij}$ reduces to μ_* , if $i = j$.

Since the stellar path length correction was envisioned and applied for Earth's atmosphere models, we explore in Section 4.4 the effect of such a correction to radiative transfer calculations for a case of a hot Jupiter and a super-Earth.

2.5. Scattering Correction for the Two-stream Method

Two-stream radiative transfer models possess an accuracy deficit compared to multistream radiative transfer methods. In a

meticulous study, Kitzmann et al. (2013) showed that the hemispheric two-stream radiative transfer method (e.g., Heng et al. 2014), as employed in HELIOS, overestimates the scattering and transmission of stellar radiation through cloud decks by up to 20%. More specifically, the two-stream method overestimates the net greenhouse effect of CO₂ clouds, which are strongly scattering in the thermal wavelengths. Thus, using a too-simplistic radiative transfer method may lead to wrong temperature estimates and corresponding atmospheric conditions, e.g., as happened for studies of the early Mars climate (Kitzmann 2016). Yet two-stream models are still prevalent, as more sophisticated radiative transfer methods often prove to be too computationally challenging to be efficiently used in large-scale climate simulations. Hence, there exist a number of tweaks to enhance the scattering behavior of two-stream models, like the δ -Eddington (Joseph et al. 1976) or the two-stream source function methods (Toon et al. 1989). Recently, Heng & Kitzmann (2017) introduced a correction factor E into the two-stream coupling coefficients ζ_{\pm} (see Section 2.1.2), which they calibrated to reproduce the results of a 32-stream DISORT code (Hamre et al. 2013). Later, Heng et al. (2018) developed a new and improved formalism consistently embedding the correction factor E into the two-stream equations. This correction factor depends only on the single-scattering albedo ω_0 and the scattering asymmetry parameter g_0 . Conveniently, all scattering problems can be reduced to those two quantities, which means that a model equipped with E can treat any atmospheric condition imaginable. The latest version of HELIOS includes Heng et al.'s (2018) version of the correction factor E through the fitting function given by their Equation (31).

We test the two-stream method, including the scattering correction versus the standard method, in Section 4.5.

3. Numerical Setup

3.1. Chemical Abundances

The atmospheric mixing ratios are obtained with the FastChem code, which reliably calculates the thermochemical equilibrium abundances of around 550 gas phase species for temperatures between 100 and 6000 K (Stock et al. 2018). We use the solar elemental abundances as stated in Table 1 of Asplund et al. (2009) throughout this study, unless otherwise stated. For nonsolar metallicities, we adjust all elements heavier than He, and for nonsolar C/O ratios, we keep O at solar value and adjust C accordingly.

We post-process the equilibrium abundances with the effects of condensation; i.e., we remove species in the parameter space where their gas abundance is expected to decrease drastically due to their own condensation or participation in condensate dust species. See Appendix B for more details.

3.2. Opacities

We have massively extended our list of opacity sources since Malik et al. (2017); see Table 1. The new version of our in-house opacity calculator HELIOS-K (Grimm & Heng 2015) is able to automatically download and calculate the spectral line lists from the ExoMol, HITRAN/HITEMP, and Kurucz online databases, which facilitates the inclusion of new opacities significantly. In this study, we include the main spectroscopically active and atmospheric abundant molecules, as expected in atmospheres with temperatures from a few hundred

⁹ We acknowledge that it is challenging to relate a pressure with the observed radius (Heng & Kitzmann 2017); thus, the indicated pressure is merely a “best-guess” assumption.

Table 1
Opacities/Scattering Cross Sections Used in This Work

Name	Online Source	Reference
Main Infrared Absorbers		
H ₂ O	ExoMol ^a	Barber et al. (2006)
CO ₂	HITEMP ^b	Rothman et al. (2010)
CO	ExoMol	Li et al. (2015)
CH ₄	ExoMol	Yurchenko & Tennyson (2014)
O ₂	HITRAN ^c	Gordon et al. (2017)
NO	ExoMol	Wong et al. (2017)
SO ₂	ExoMol	Underwood et al. (2016)
NH ₃	ExoMol	Yurchenko et al. (2011)
OH	HITEMP	Rothman et al. (2010)
HCN	ExoMol	Harris et al. (2006)
C ₂ H ₂	HITRAN	Gordon et al. (2017)
PH ₃	ExoMol	Sousa-Silva et al. (2015)
H ₂ S	ExoMol	Azzam et al. (2016)
SO ₃	HITRAN	Gordon et al. (2017)
PO	ExoMol	Prajapati et al. (2017)
Metal/Other Hydrides		
SiH	ExoMol	Yurchenko et al. (2018)
CaH	ExoMol	Yadin et al. (2012)
MgH	ExoMol	Yadin et al. (2012)
NaH	ExoMol	Rivlin et al. (2015)
AlH	ExoMol	Yurchenko et al. (2018)
CrH	ExoMol	Burrows et al. (2002b)
Metal Oxides		
VO	ExoMol	McKemmish et al. (2016)
TiO	VALD ^d	Ryabchikova et al. (2015)
AlO	ExoMol	Patrascu et al. (2015)
SiO	ExoMol	Barton et al. (2013)
CaO	ExoMol	Yurchenko et al. (2016)
CIA		
H ₂ -H ₂	HITRAN	Richard et al. (2012)
H ₂ -He	HITRAN	Richard et al. (2012)
Atoms and Ions		
Na and K	Kurucz ^e	Kurucz (2011), Burrows et al. (2000), Burrows & Volobuyev (2003), P. E. Cubillos et al. (2019, in preparation)
H ⁻		John (1988)
Scattering Cross Sections		
H ₂		Sneep & Ubachs (2005)
H		Lee & Kim (2004)

Notes.^a exomol.com^b hitran.org/hitemp/^c hitran.org/^d vald.astro.uu.se/^e kurucz.harvard.edu/

to several thousand K. We divide our opacities into the main infrared absorbers, metal or other hydrides, metal oxides, Na and K,¹⁰ and H⁻. We use this division in Section 4.2 to investigate the spectroscopic impact of these absorbing species. For the atmospheric model grid, we use all of the opacity

¹⁰ We elaborate on the calculation of the Na and K opacities in Appendix A in detail.

sources listed in Table 1. Figure 3 shows the included opacities for one temperature and pressure weighted with their respective equilibrium mixing ratio. The molecular opacities are computed at a resolution of 10⁻² cm⁻¹, the Na and K opacities at 10⁻¹ cm⁻¹, and H⁻ at 10 cm⁻¹. The calculation of the alkali metals is described in detail in Appendix A. For all other molecules, we use a Voigt profile, and, due to the absence of a first-principles theory for pressure broadening, we adopt the community procedure of an ad hoc truncation of the line wings at 100 cm⁻¹ from the line center. For the opacities with data from the ExoMol database, we include the default broadening as provided in their online library. For the HITRAN/HITEMP opacities, we use their self-broadening parameters.

Lastly, we are aware that we are missing the opacities of collision-induced absorption (CIA) H₂-H₂ blueward of 1 μm (Borysow et al. 2001; Borysow 2002). They play an insignificant role for hot, irradiated atmospheres because other opacity sources present, such as the alkali metals or the metal hydrides and oxides, assume the role of the dominant shortwave absorbers. Furthermore, CIA absorption generally only becomes important in the deep atmosphere, $P \gtrsim 10$ bars, as it scales with the pressure squared. However, at these depths, the convective region usually begins. That means that the atmosphere there is optically thick and thus not visible in the planetary emission, and the according temperatures are given by the adiabatic lapse rate and not by radiative equilibrium.

3.3. Iteration and Post-processing

For the iterative runs, i.e., to find the temperature profile in radiative–convective equilibrium, we employ the κ -distribution method with a correlated- κ approximation as described in Malik et al. (2017). We use 300 wavelength bins over a range of 0.33–10⁵ μm. Each bin contains 20 Gaussian points where independent flux calculations are performed. With the addition of strong shortwave absorbers, occasional discontinuities in the converged temperature profile may occur. This is countered by a temperature-smoothing algorithm (see Appendix C). Furthermore, there is now the option to bypass the κ -distribution method and sample the opacities at the discrete flux wavelength values. This approach, commonly called *opacity sampling*, is used in this study to generate high-resolution spectra (8263 wavelength bins) by post-processing a given temperature profile. To elucidate on our terminology, we regard the difference between “*opacity sampling*” and “*line-by-line*” as a matter of sampling resolution. When the number of sampling points greatly exceeds the number of spectral lines considered, the computation qualifies as being *line-by-line*. When the number of sampling points is comparable to or smaller than the number of lines, as it is in our case, then one is performing *opacity sampling*.

4. Results

In this section, we expose HELIOS to a radiative transfer model intercomparison, conduct a number of working tests, and present self-consistent atmospheric models for self-luminous and irradiated planets.

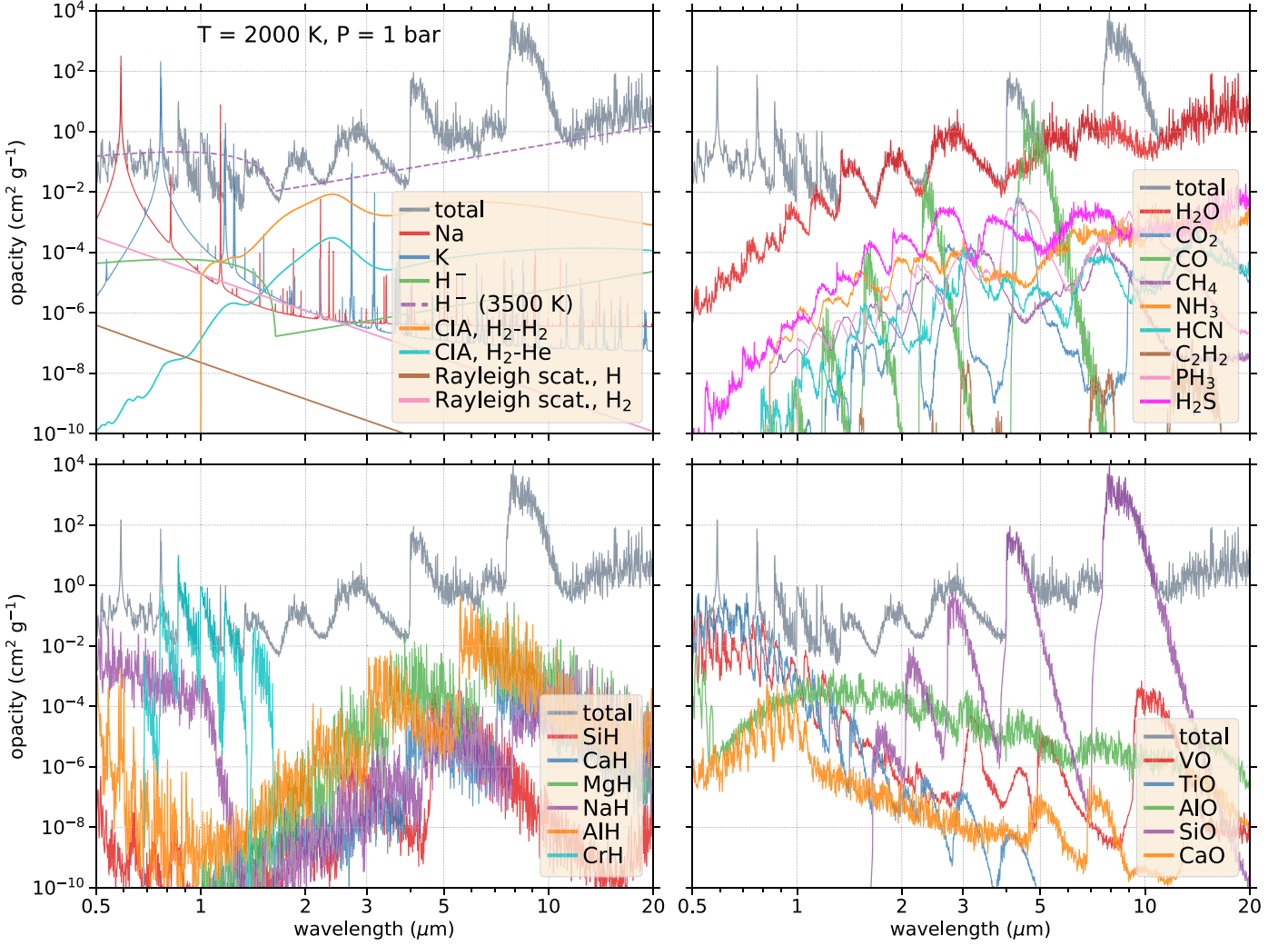


Figure 3. Opacity vs. wavelength for all opacity/extinction sources used in this work. We show an excerpt of the opacity table for one temperature and pressure. Each opacity is weighted by its chemical equilibrium mass mixing ratio. Depicted are the atomic/ion, CIA, and scattering opacities (top left), the main infrared absorbers (top right), metal and other hydrides (bottom left), and metal oxides (bottom right). Each plot also shows the total gas opacity. The displayed opacities are downsampled in resolution for clarity. See Table 1 for a full list of species.

4.1. Model Intercomparison

4.1.1. Exo-REM, petitCODE, and ATMO

In a series of benchmark tests, Baudino et al. (2017) compared the three radiative transfer models Exo-REM (Baudino et al. 2015), petitCODE (Mollière et al. 2015), and ATMO (Amundsen et al. 2014) to identify troublesome model parameters and how these may affect simulated atmospheres. For this purpose, they aligned the three codes in terms of chemistry, opacity line lists, and the treatment of spectral lines and investigated the effect of each of those aspects. As such an intercode comparison goes beyond the scope of this study, we limit our comparison to the self-consistent calculation of the four therein explored planets: the self-luminous GJ 504b and VHS 1256-1257b, the irradiated super-Earth GJ 436b, and the hot Jupiter WASP-12b.¹¹ In order to mimic their setup, we limit ourselves to the following opacities: H_2O , CO_2 , CO , CH_4 , NH_3 , PH_3 , the alkali metals Na

and K , and CIA from $\text{H}_2\text{-H}_2$ and $\text{H}_2\text{-He}$. Furthermore, we include Rayleigh scattering for H_2 and H .

Using their planetary parameters and numerical setup, we self-consistently calculate the temperature profiles and emission spectra of the aforementioned planets; see Figure 4, top left and right panels, respectively. The temperature profiles of the self-luminous planets agree very well. Also, for GJ 436b, the temperatures are consistent among all models, although HELIOS leads to slightly warmer deep atmospheric layers (pressure < 1 bar). In general, the temperature differences are minuscule, and thus it is not surprising that the corresponding emission spectra for these three planets also match very well. In fact, we are surprised about such a high level of agreement, as there are still differences in the treatment of opacities between HELIOS and the other models. Not only do we use different line lists but, particularly, the calculation of the far wings deviates. They employ a pure Voigt profile for the Na and K resonance lines, whereas our line wings are influenced by Burrows & Volobuyev's (2003) formalism. This discrepancy is particularly visible in the submicron wavelength range, where the far wings of the alkali resonance lines dominate the

¹¹ As Exo-REM is not built for external irradiation, its models are missing for the latter two planets.

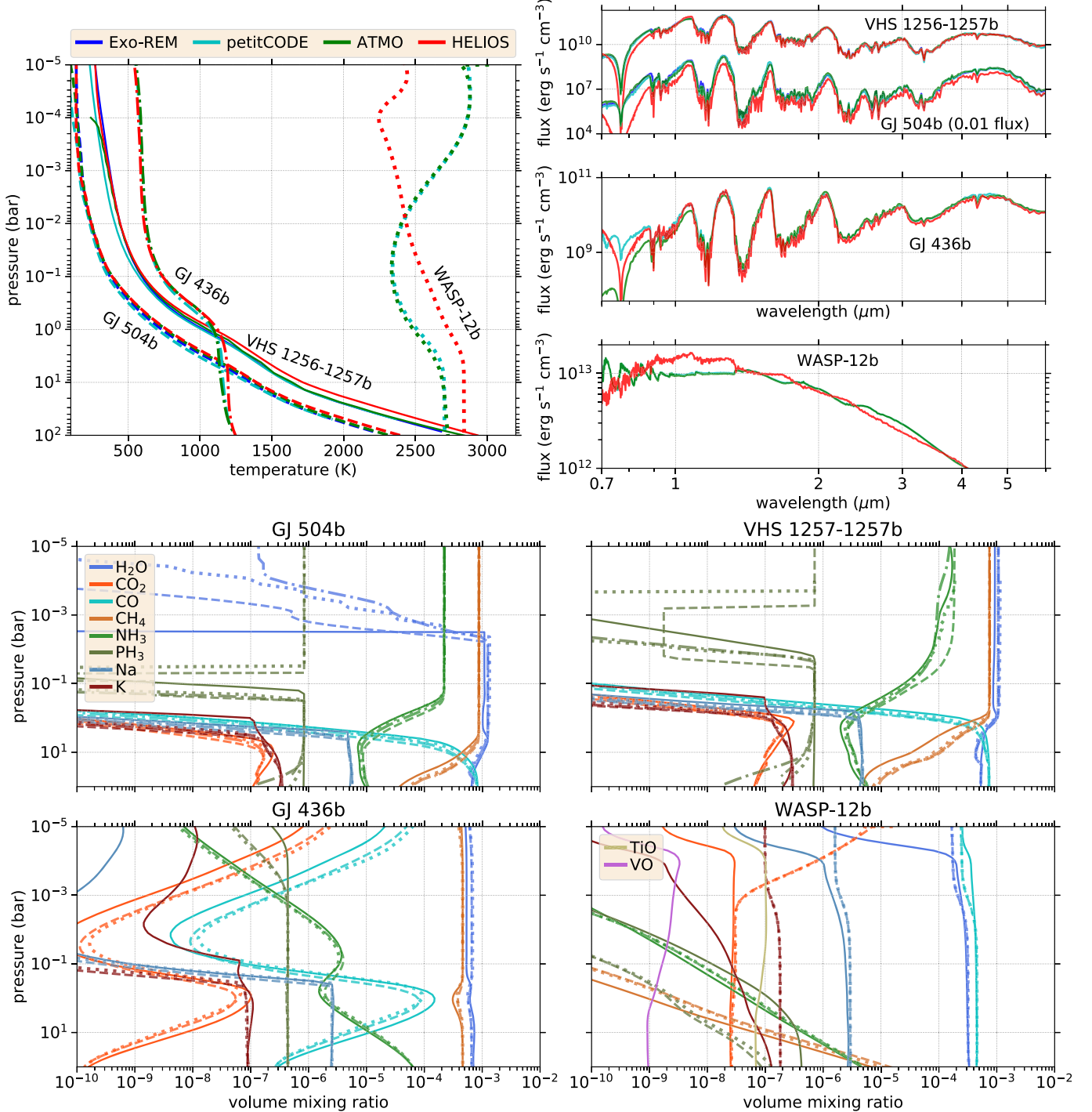


Figure 4. Comparison of self-consistently calculated atmospheres by Exo-REM, petitCODE, ATMO, and HELIOS for the planets GJ 504b, VHS 1256-1257b, GJ 436b, and WASP-12b. Top left panel: temperature profiles in radiative-convective equilibrium. Top right panels: emission spectra corresponding to the temperature profiles on the left. The flux of GJ 504b is multiplied by 0.01 to help distinguish between the depicted spectra. Bottom four panels: vertical abundance profiles for the models shown in the top panels. The abundances of HELIOS, petitCODE, ATMO, and Exo-REM are represented by solid, dashed, dotted, and dashed-dotted lines, respectively. The color scheme is the same in the four bottom panels. Since Exo-REM only handles nonirradiated planets, its model data are missing for GJ 436b and WASP-12b. Finally, the abundances of TiO and VO, as used for WASP-12b, are not provided in Baudino et al. (2017) and are shown only for HELIOS.

absorption. Note that the shown spectra have been downgraded to the same resolution to facilitate a comparison.

A special case is WASP-12b, because they additionally include TiO and VO as absorbers for this planet. Although we also extend our opacity list with these two molecules, we obtain a substantially different temperature profile and emission spectrum. We cannot reproduce their large temperature

inversion and are consequently missing their strong emission features in the optical. We speculate that the difference must be caused by differences in the TiO and VO line lists. Incomplete line lists or erroneous line strengths may both lead to stark differences in the shortwave heating of the upper atmosphere.

In Figure 4 (bottom panels), we show the corresponding vertical abundance profiles for the four planets used in the

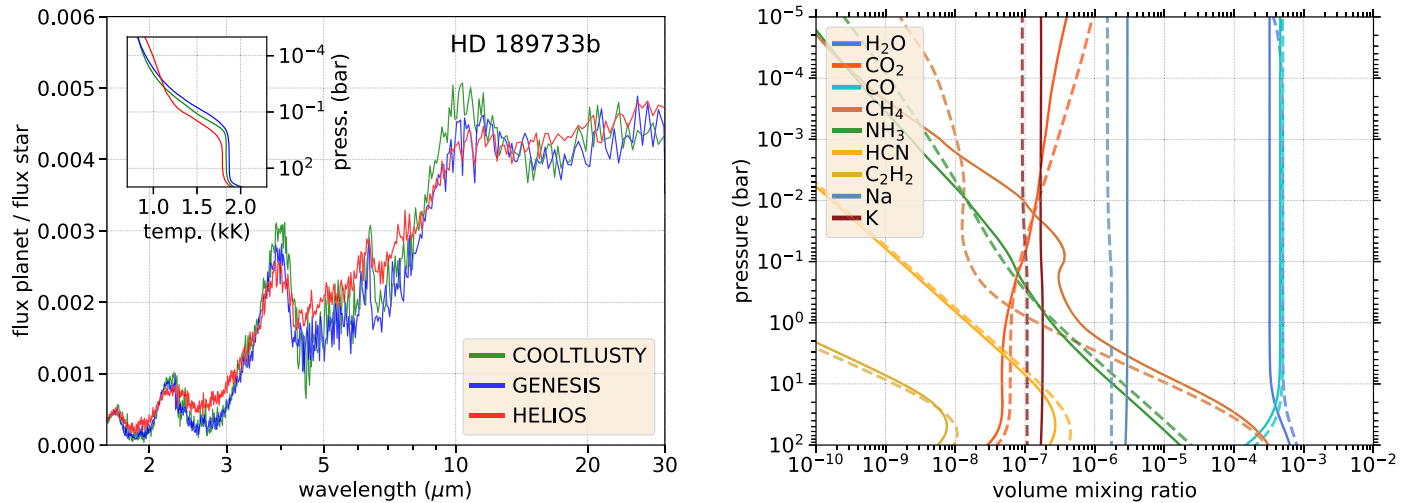


Figure 5. Left panel: comparison of the secondary eclipse spectrum and dayside temperatures in radiative–convective equilibrium (inlaid) of HD 189733b modeled with COOLTLUSTY, GENESIS, and HELIOS. The spectra are downsampled in resolution for clarity. Right panel: vertical abundances from the HELIOS (solid lines) and GENESIS (dashed lines) models shown on the left. The dominant absorbing species are H_2O and CO in the near-infrared and Na and K at shorter wavelengths.

models. Even though the models are based on the same elemental abundances of Asplund et al. (2009), the exact molecular abundances depend on the choice of solving method, the utilized thermochemical data, and the size of the chemical network considered. Baudino et al. (2017) gave an overview of the chemistry in `petitCODE`, ATMO, and Exo-REM in their Section 2.2. We hypothesize three main reasons for the discrepancies in the chemical abundances between the models. First, some differences in the abundances stem directly from differences in the temperature profiles. This is best visible for WASP-12b, for which the found temperature profiles differ the most. Second, the removal of gas species due to condensation is modeled differently by each of the models. Critical to this issue is at which temperature condensation of the gas species occurs and whether the species in question might be removed indirectly by the formation of a dust compound. Unlike the other models, Exo-REM includes a “cold trap” by removing species located above the one where its condensation curve is crossed. We describe the method of how we apply condensation in Appendix B. Third, we include ions in our thermochemical network, which means that at higher temperatures, neutral species are depleted due to ionic transitions. Without this depletion, the number of neutral species may be overestimated. This explains, e.g., the discrepant abundances of K for WASP-12b between the models.

4.1.2. COOLTLUSTY and GENESIS

Next, we join in Gandhi & Madhusudhan’s (2017) model comparison of their new radiative model GENESIS with the results of Burrows et al. (2008) for HD 189733b. The latter used the COOLTLUSTY model, which has a long-standing history of exoplanet applications. The most detailed description of the vast array of opacity sources included in COOLTLUSTY is given in Sharp & Burrows (2007). Many fewer opacities are included in GENESIS, namely, H_2O , CO_2 , CO , CH_4 , NH_3 , HCN , C_2H_2 , Na , K , and CIA $\text{H}_2\text{--H}_2$ and $\text{H}_2\text{--He}$. We use the latter batch of GENESIS’s opacities for this particular comparison. Furthermore, we use their planetary parameters to obtain the same effective dayside temperature and include a

stellar blackbody to avoid potential discrepancies due to a mismatched stellar model.

Figure 5 (left panel) shows the synthetic secondary eclipse spectra together with the corresponding temperature profiles in radiative–convective equilibrium according to each model. The shown spectra are downsampled to a common resolution to facilitate a qualitative comparison. In general, HELIOS’s spectrum matches the other two well, with the largest difference being somewhat smaller peaks and troughs in the features between 2 and $10\ \mu\text{m}$. This is a consequence of the smaller temperature difference between the upper and lower atmosphere, which directly translates to the magnitude of spectral features. Also, in our case, the photosphere is located slightly deeper as compared to the other models. Yet the global difference between HELIOS and COOLTLUSTY appears only slightly larger than the difference between GENESIS and COOLTLUSTY. As in the last subsection, we argue that the most likely causes for the discrepancies between the models stem from the opacities. An in-depth comparison of the radiative transfer method, which exceeds the scope of this study, would need to eliminate the following problematic factors that are present here: different sets of employed opacities, different line lists, different spectral line-wing treatments (see Baudino et al. 2017), and differences in the stellar spectrum (which directly affect secondary eclipse spectra). Until those factors are brought to a common denominator, an absolute convergence of the models remains elusive or coincidental.

In Figure 5 (right panel), the vertical abundance profiles as obtained in the HELIOS (solid lines) and GENESIS (dashed lines) models are shown. The main near-infrared absorbers are H_2O and CO , and CH_4 in the bottom atmosphere. The relatively abundant alkali metals, Na and K , provide the shortwave absorption and thus play an important role for the extinction of starlight. We attribute the main discrepancies in the abundance profiles between HELIOS and GENESIS to the size of the employed chemical network and differences in the atmospheric temperatures. The latter cause is particularly noticeable in the case of CH_4 , as its abundance substantially decreases with temperature T if $T \gtrsim 850\ \text{K}$. The discrepancy in the H_2O abundance may stem from using a slightly different

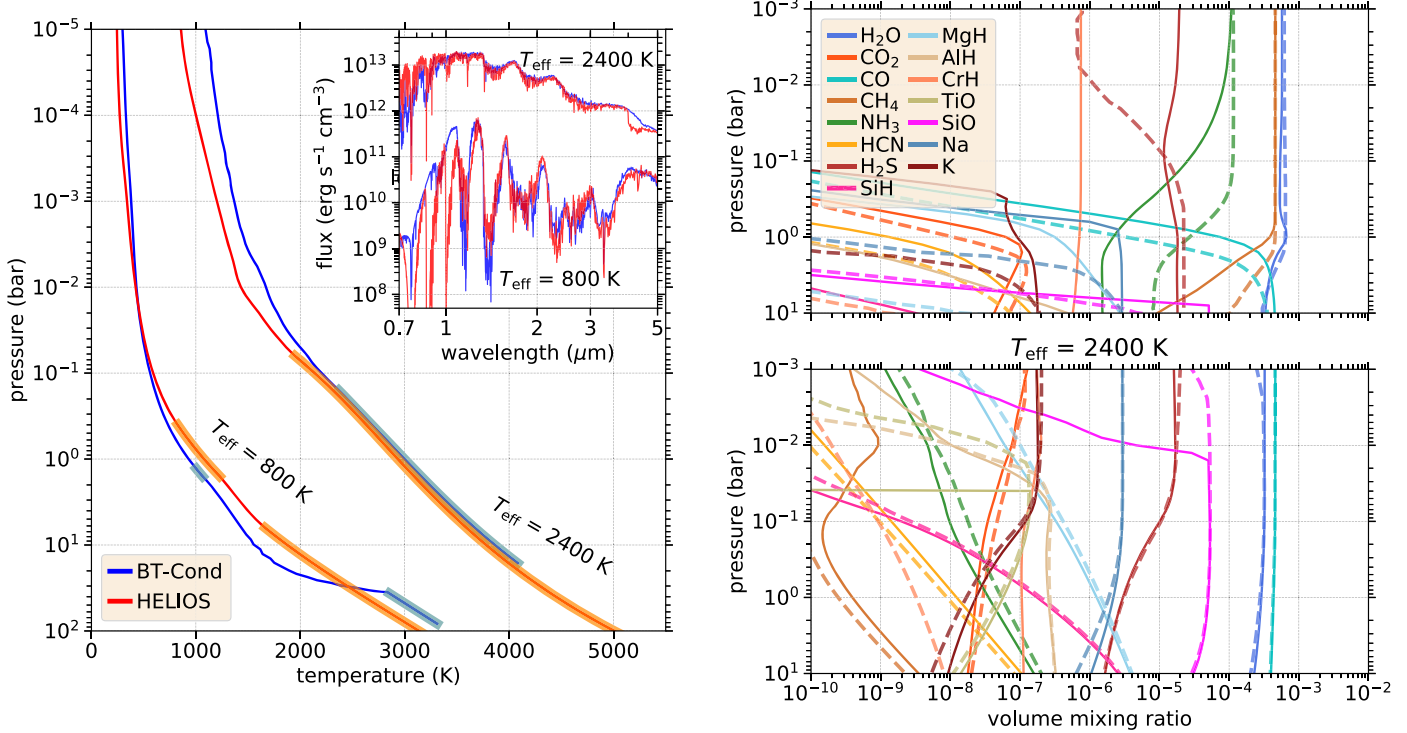


Figure 6. Left panel: comparison of temperatures in radiative–convective equilibrium and the corresponding emission spectra (inlaid) calculated with **HELIOS** and from the **BT-Cond** models. Two self-luminous planets with effective temperatures of 800 and 2400 K and a surface gravity of 10^4 cm s^{-2} are explored. Convective zones are displayed as broader lines. Right panels: vertical abundances from the **HELIOS** (solid lines) and **BT-Cond** (dashed lines) models shown on the left. The color scheme is the same in both panels. The abundances of the included species VO, NaH, C₂H₂, PH₃, CaO, and CaH are not shown due to clarity, since they are comparatively low for both explored cases ($\lesssim 10^{-7}$).

value for the solar elemental abundances of carbon and oxygen, $\text{C}/\text{O}_{\text{HELIOS}} = 0.55$ and $\text{C}/\text{O}_{\text{GENESIS}} = 0.5$. Also, in the larger chemical network used in **HELIOS**, the oxygen atoms are divided among more oxygen-bearing species, which leads to a decrease in the H_2O abundance. Lastly, since the equilibrium chemistry formulae in **GENESIS** do not include the alkali metals, they appear to use the solar elemental abundances for Na and K. This approach returns somewhat smaller values than what we have.

4.1.3. *BT-Cond*

There are two reference models that stand out when it comes to atmospheres of self-luminous planets or brown dwarfs: the **COOLTLUSTY** models and the **PHOENIX** models. As we compared to **COOLTLUSTY** in last subsection, we turn here toward **PHOENIX**. With this code, numerous atmospheric grids have been published with different flavors of ingredients over the past 20 yr (e.g., Allard et al. 2001; Baraffe et al. 2003; Allard et al. 2011; Lothringer et al. 2018). The newest and most up-to-date members of this series are the **BT-Cond** (only gas opacities) and **BT-Settl** (includes a cloud model) atmospheric grids (Allard et al. 2012a). We choose **BT-Cond** as a comparison partner, since we do not model clouds. As **BT-Cond** includes a vast array of opacities at our disposal, we too employ the full array of opacities at our disposal, as listed in Table 1. We take as test objects a colder and a hotter nonirradiated planet with effective temperatures of 800 and 2400 K, respectively. We set the surface gravity to 10^4 cm s^{-2} and compare the self-consistently calculated radiative–convective temperature profiles and the corresponding emission spectra;

see Figure 6 (left panel). We further analyze the appearance of convective zones (shown as broader lines). We find that the temperatures in the hotter test case agree rather well with the only deviation in the upper atmosphere, where **HELIOS** predicts colder temperatures. However, being optically thin, this region plays only a minor role for the spectroscopic appearance of the planet and manifests itself as slightly weaker emission at wavelengths larger than $1.3 \mu\text{m}$. The deep convective zone is almost identical for both models, which is the relevant aspect for the coupling to interior models. The colder planet exhibits a somewhat warmer photosphere and colder deeper layers (pressure $< 1 \text{ bar}$) in the **HELIOS** version. Interestingly, the **BT-Cond** model exhibits a significantly larger temperature gradient in the deep layers, which would be unstable and corrected with our employed equation of state. We attribute this discrepancy to the calculation of atmospheric entropy. On the other hand, the upper atmospheric temperatures are consistent, and both models even agree on the detached convective zone, although it is larger in the **HELIOS** model. Important for the coupling with interior models is the fact that the deep convective zones are somewhat shifted. According to the lower deep temperature in the **HELIOS** model, the spectral emission is somewhat weaker below $1.3 \mu\text{m}$ than in the **BT-Cond** model. Interestingly, we see strong CrH absorption features at 0.9 and $1 \mu\text{m}$ that are missing in the **BT-Cond** model. Indeed, observing the vertical abundance profiles of the two models (Figure 6, top right panel), the abundance of CrH is strongly muted for **BT-Cond** compared to **HELIOS**. We attribute this difference to a condensation effect implemented in **BT-Cond** but missing in **HELIOS**. Another interesting case is SiO. Namely, the temperatures of the upper atmosphere in

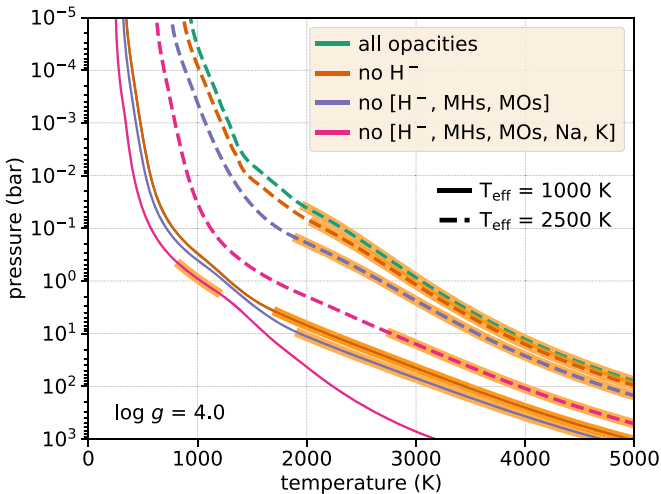


Figure 7. Temperature profiles in radiative–convective equilibrium for two self-luminous planets with effective temperatures of 1000 and 2500 K and a surface gravity of 10^4 cm s^{-2} . The effect of using different samples of opacity sources on the calculated temperatures is explored. Convective zones are displayed as broader orange lines. The solid green line is perfectly covered by the solid brown line.

the two models are located below (HELIOS) and above (BT-Cond) the condensation temperature of MgSiO_3 , responsible for depleting SiO . Also, other species, like NH_3 and H_2S , show considerable differences in their abundance between the two models, which could be caused by differences in either the temperatures and/or thermochemical data and the chemical network utilized.

4.2. Impact of the Opacities on Temperatures

We now present a few numerical tests to shed light on the impact of some of the new features included in HELIOS. In this section, we investigate the effects of different opacity sources on converged atmospheric temperature profiles after running the iteration for radiative–convective equilibrium.

For these tests, we use different opacity tables for our calculations. The tables consist of varying sets of opacities that are premixed using the same chemical network in order to single out the effect of missing opacities while keeping the molecular abundances the same.

1. Sample A includes all opacities at our disposal, as listed in Table 1.
2. Sample B is equal to sample A minus the H^- continuum opacity.
3. Sample C is equal to sample B minus the metal and other hydrides and metal oxides, as shown in the bottom left and right panels of Figure 3. Effectively, that means we are removing SiH , CaH , MgH , NaH , AlH , CrH , TiO , VO , AlO , SiO , and CaO .
4. Sample D is equal to sample C minus the Na and K opacities. This removes the last strong shortwave absorbers from the opacity pool.

The first setup consists of two self-luminous planets with effective temperatures of 1000 and 2500 K and a surface gravity of 10^4 cm s^{-2} ; see Figure 7. For the colder planet, samples A and B lead to the identical temperature profile. Sample C leads to somewhat cooler temperatures, and sample D is markedly different. In the latter case, there are no

shortwave absorbers left, so the hot bottom atmosphere cools too efficiently to be convectively unstable. Conversely, including all available opacities leads to the hottest temperatures, since having more absorbing species increases the optical depth and moves the photosphere upward. Subsequently, the lower atmosphere emits radiation less efficiently, which drives the temperatures up. The hotter planet shows similar trends, even more pronounced. Here the addition of H^- has a noticeable effect on the temperature. The hotter planet exhibits convective zones extending to lower pressures compared to the colder planet, which is likely due to more spectral lines being active, increasing the overall optical depth. As discussed in Section 1, the entropy found in the deep convective zones is of special interest for the coupling with interior models. Hence, we list the obtained values for the entropies S in the conducted runs. For the colder planet, the entropy in the model with sample A is $S_A = S_B = 8.95$ and $S_C = 8.74$. There is no deep convective zone when using sample D. The hotter planet models lead to $S_A = 11.23$, $S_B = 10.99$, $S_C = 10.53$, and $S_D = 9.46$, with a modeling accuracy of $\Delta S \approx 0.02$. The values for S are given in units of the Boltzmann constant.

The second setup consists of the following irradiated planets covering a broad range of effective dayside temperatures: GJ 1214b ($T_{\text{eff}} = 721 \text{ K}$), HD 189733b ($T_{\text{eff}} = 1465 \text{ K}$), WASP-12b ($T_{\text{eff}} = 3013 \text{ K}$), and KELT-9b ($T_{\text{eff}} = 4528 \text{ K}$). We also include an internal temperature of 85 K. For each of these planets, we explore the diversity of dayside temperatures obtained when using the various samples of opacity sources. Our findings are shown in Figure 8. Two global statements can be made immediately. First, the temperature profiles vary substantially depending on the employed opacities. Second, this variance increases with stellar irradiation and effective planetary temperature. For GJ 1214b and HD 189733b, samples A and B lead to the same temperatures. Samples C and D lead to cooler upper and warmer lower atmospheres, resulting in a larger atmospheric greenhouse effect. Sample D additionally moves the stellar photosphere downward due to the lack of shortwave absorbers. With WASP-12b and KELT-9b, we move to effective temperatures beyond 3000 K, where H^- opacity starts to have a strong effect. Because H^- introduces a very strong continuum opacity throughout all wavelengths (see Figure 3), it makes the temperature profile more isothermal. In addition, the metal hydrides and oxides play a strong role in this regime, leading to minor (WASP-12b) or major (KELT-9b) temperature inversions. In the case of KELT-9b, because the stellar irradiation is so strong, even Na and K suffice to lead to two separate temperature inversions. In fact, we expect nonmonotonic temperature profiles with multiple inversions to be naturally occurring in very hot atmospheres (see Section 4.3).

In conclusion, we find that missing opacities in models may lead to stark temperature discrepancies. We thus recommend employing a list of opacity sources as complete as possible to avoid erroneous temperature predictions, an error that directly propagates into the strength of the spectroscopic emission features. More specifically, we find the inclusion of metal hydrides, oxides, and H^- imperative to obtaining accurate temperatures. We remark that in very hot atmospheres, atomic or ion species like Fe , Mg , Al or Fe^+ , Mg^+ , Ca^+ are expected to play a significant role as well, due to their high abundance and vast number of spectral lines in the optical and near-infrared (Kitzmann et al. 2018). We further remark that Fe ,

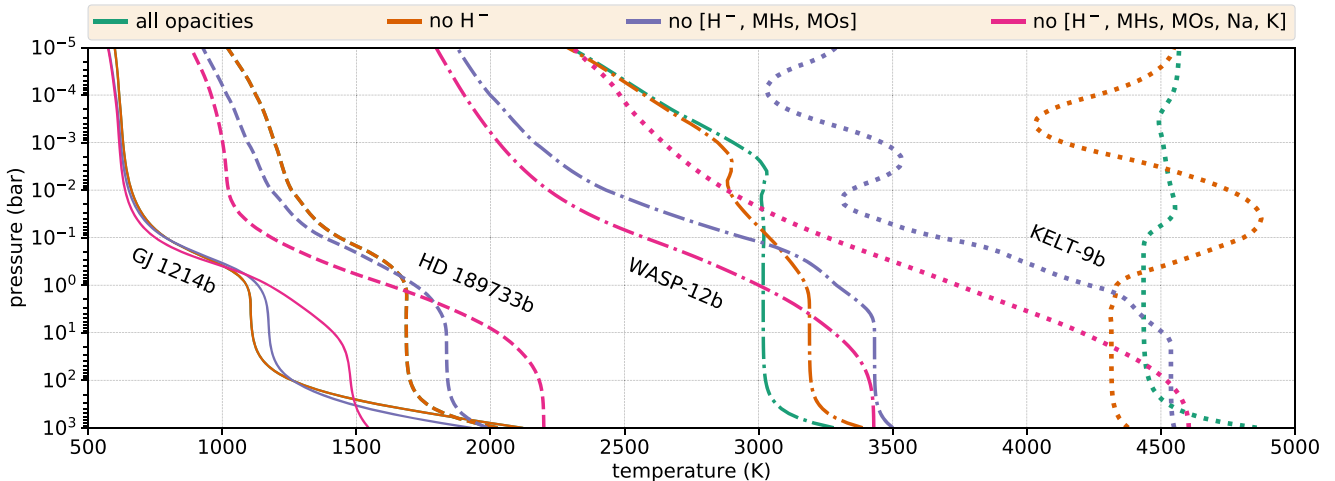


Figure 8. Dayside temperature profiles in radiative–convective equilibrium for the planets GJ 1214b ($T_{\text{eff}} = 721$ K), HD 189733b ($T_{\text{eff}} = 1465$ K), WASP-12b ($T_{\text{eff}} = 3013$ K), and KELT-9b ($T_{\text{eff}} = 4528$ K). The effect of different samples of opacity sources on the calculated temperatures is shown. The discrepancy between models increases with planetary effective temperature as the metal oxides, hydrides, and H^- start to dominate the stellar flux absorption. The green profile is perfectly covered by the brown profile in the two colder cases.

Fe^+ , and Ti^+ were recently observationally confirmed in the atmosphere of the ultrahot Jupiter KELT-9b (Hoeijmakers et al. 2018), reinforcing the notion of the prevalent existence of metals in very hot atmospheres.

We will investigate the impact of more atoms and ions on self-consistent radiative transfer calculations in a future study.

4.3. Nonmonotonic Temperature Profiles

As seen in the previous section, we find that for hotter planets with effective temperatures over 2000 K, nonmonotonic temperature profiles are not the exception but the norm. In this regime, sufficiently high temperatures activate a multitude of rovibronic transitions that generate billions of spectral lines belonging to many different species that cause complex extinction patterns for both stellar and planetary radiation. Even more, with planets orbiting cool M dwarfs or ultrahot Jupiters exhibiting temperatures like K stars, the wavelengths of incoming irradiation and local thermal emission may heavily overlap, eroding the classical shortwave and longwave paradigm. In this sense, we feel that the question of whether a planetary atmosphere exhibits a temperature inversion or not (e.g., Fortney et al. 2008) is ill-posed, as there may be small or large and one or several inversions appearing in higher or lower altitudes.

We conduct a numerical test to explore the origins of nonmonotonic temperature profiles. As a test setup, we choose to model the dayside of KELT-9b and employ our full opacity list without H^- . As seen in Figure 8, this leads to a temperature profile with two large temperature inversions. In order to better explore the wavelength-dependent opacity effect, we use, for this test only, opacities calculated at a fixed pressure and temperature of $P = 1$ bar and $T = 4500$ K. With this simplification, the photospheric pressure at which the optical depth τ equals unity is given directly by

$$P = g/\kappa, \quad (28)$$

where g is the surface gravity and κ is the wavelength-dependent opacity function. For the following demonstration, it is useful to know that the stellar irradiation of KELT-9 and the

planetary thermal emission peak at 0.3 and 0.7 μm , respectively.

The converged temperature profile is shown in the left panel and the contribution function in the right panel of Figure 9. The latter is overlaid by the location of the photosphere, given by Equation (28). Due to the use of the κ -distribution method, each wavelength bin contains a range of unordered opacities that returns a range of photospheric pressures. Now, we ask the question of which opacity bands and spectral lines are responsible for which features of the temperature profile. To this end, we manually switch off or strongly decrease opacities in certain wavelengths and study the effect on the temperature profiles. We elucidate our findings by focusing on individual temperature regions, which are connected by lines A–E to the pressure layers and opacity bands they are most affected by.

1. A. The temperature inversion above¹² 10^{-6} bars is caused by the Na resonance doublet. Stellar radiation is absorbed by the line center, resulting in an increase of temperature until the thermal radiation emits sufficiently at 0.59 μm to counter the stellar energy deposition.
2. B. The dip in temperatures around 10^{-6} bars is mainly caused by efficient cooling through the SiO band at 9 μm , with the band at 4.5 μm playing a minor part. The layers at this height cool down until the cooling is countered by stellar heating through the other K and Na line peaks at $\lesssim 1 \mu\text{m}$.
3. C. The inversion around and below 1 mbar is due to the absorption of stellar radiation by strong shortwave bands of SiH and AlH between 0.4 and 0.5 μm . This region represents the stellar photon deposition depth, as the bulk of the stellar flux is absorbed here. The temperatures here increase until the atmosphere can efficiently cool through the SiH and AlH bands as well.
4. D. At 1–10 bars lies the majority of the planetary photosphere. The temperatures are relatively low, as the gas is efficient at cooling, and only a small fraction of the stellar radiation is left at these depths. The maxima of the contribution function show that the bulk of the thermal

¹² “Above” and “below” are meant in the spatial sense, i.e., the direction of lower and higher pressure, respectively.

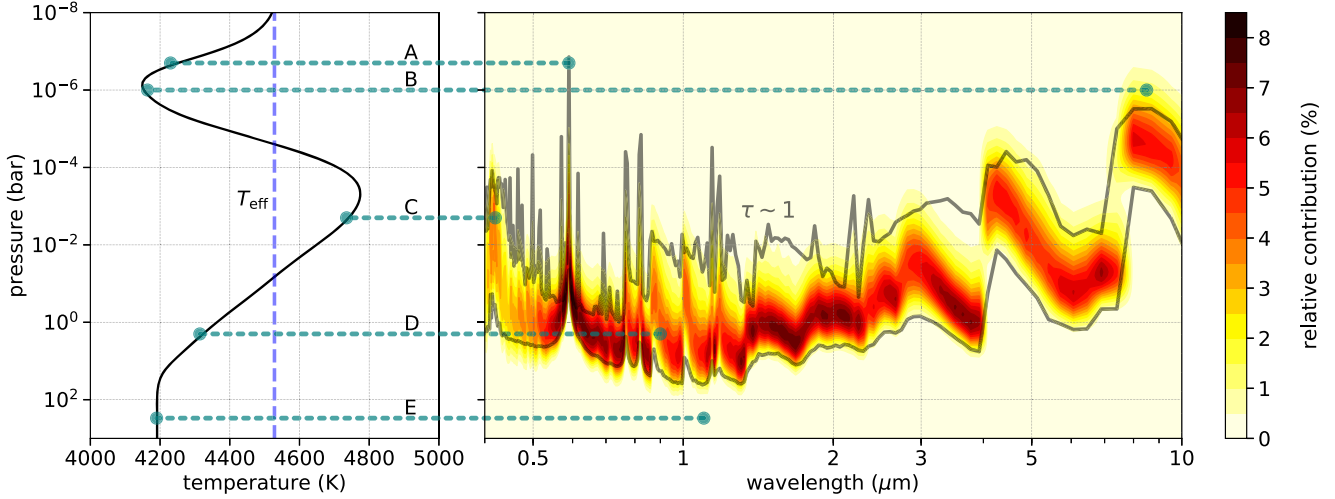


Figure 9. Left: converged dayside temperature profile of KELT-9b in a simplified test setup, where the opacities (no H^-) are held constant with altitude. Right: contribution function and photosphere (optical depth $\tau \sim 1$) vs. wavelength. Due to the use of the k -distribution method, one wavelength bin contains a range of opacities, resulting in a wider photosphere region (enclosed by two gray lines). We discuss the connection between temperatures and the pressure layers and opacity bands they are affected by (lines A–E) in the text.

emission originates from these pressures at wavelengths between 0.5 and 2 μm .

5. E. Below 100 bars, the atmosphere is optically thick to both the thermal and the stellar flux. Radiative equilibrium under these isotropic conditions manifests through an isothermal temperature profile.

In conclusion, we find that multiple temperature inversions are caused by a combination of the strong spectral bands and lines of metal oxides, metal hydrides, and the alkali metals. If these species are present in sufficient atmospheric abundances, as is expected for ultrahot planets such as KELT-9b, we expect complex temperature profiles with multiple inversions to be the common state.

However, we note once more that in this test, we used opacities calculated at one fixed value for the pressure and temperature, whereas in reality, the opacities would change throughout the atmosphere. Finally, we have neglected the H^- continuum opacity, which makes the temperatures substantially more isothermal than presented here (see Figure 8).

4.4. Effect of the Stellar Path Length Adjustment

As stated in Section 2.4, the usual practice of one-dimensional models is to use a plane-parallel grid instead of the accurate spherical geometry of planets. In doing so, the path length of photons in the atmosphere and, consequently, the optical depth are overestimated. This error can be avoided with a geometrical correction that shortens the actual stellar path length by adjusting the zenith angle depending on the location in the atmosphere. In the following, we test our implementation of the geometric correction to the stellar path for its influence on modeling exoplanetary atmospheres. We employ our full opacity list and generate temperatures in radiative–convective equilibrium and the corresponding mock spectra for the hot Jupiter HD 189733b and the super-Earth GJ 1214b. We pick each of those two as poster children for the two prevalent classes of currently characterized exoplanets. We treat the atmosphere of GJ 1214b as hydrogen-dominated, so the effects presented here should be understood as an upper limit on the significance of the path length correction. Heavier atmospheres

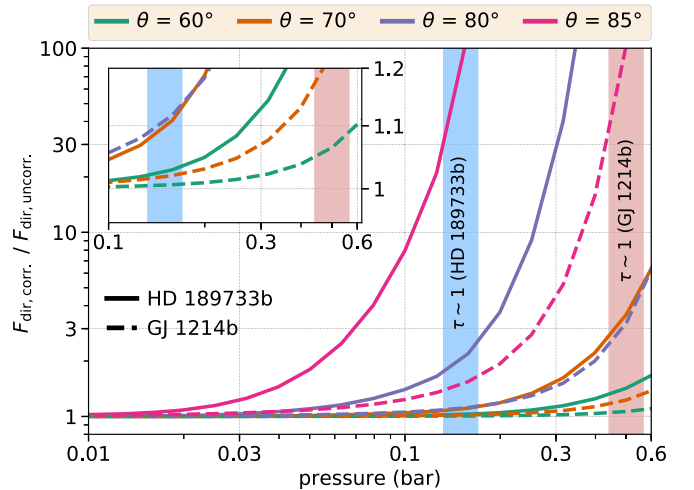


Figure 10. Vertical profile of the stellar flux ratio between models with and without the stellar path length adjustment. The ratio is shown for various zenith angles θ for both HD 189733b and GJ 1214b. The approximate photospheres (optical depth $\tau \sim 1$) of these planets are shown at the wavelength of the respective star's peak emission. Precalculated dayside temperature profiles are used for this test. Inlaid is a zoom-in of the bottom right corner.

possess a smaller scale height, diminishing the effect of a path length correction.

As a first test, we use a precalculated atmospheric temperature profile and let the direct stellar beam propagate downward, once with and once without path length correction. We show in Figure 10 the ratio of the corrected to the uncorrected stellar fluxes with increasing pressure (or atmospheric depth). High up in the atmosphere, the ratio is very close to unity but increases as the stellar photons propagate deeper. As the effect of the geometric correction is relative to the path length, the discrepancy increases with pressure. Also, the error in the uncorrected path length increases with the size of the zenith angle. The region of interest is given by the shortwave photosphere (optical depth $\tau \sim 1$), where the stellar photons are deposited and contribute to the atmospheric heating. The layers below the photosphere are left with a vanishingly small stellar flux, making an error irrelevant. In

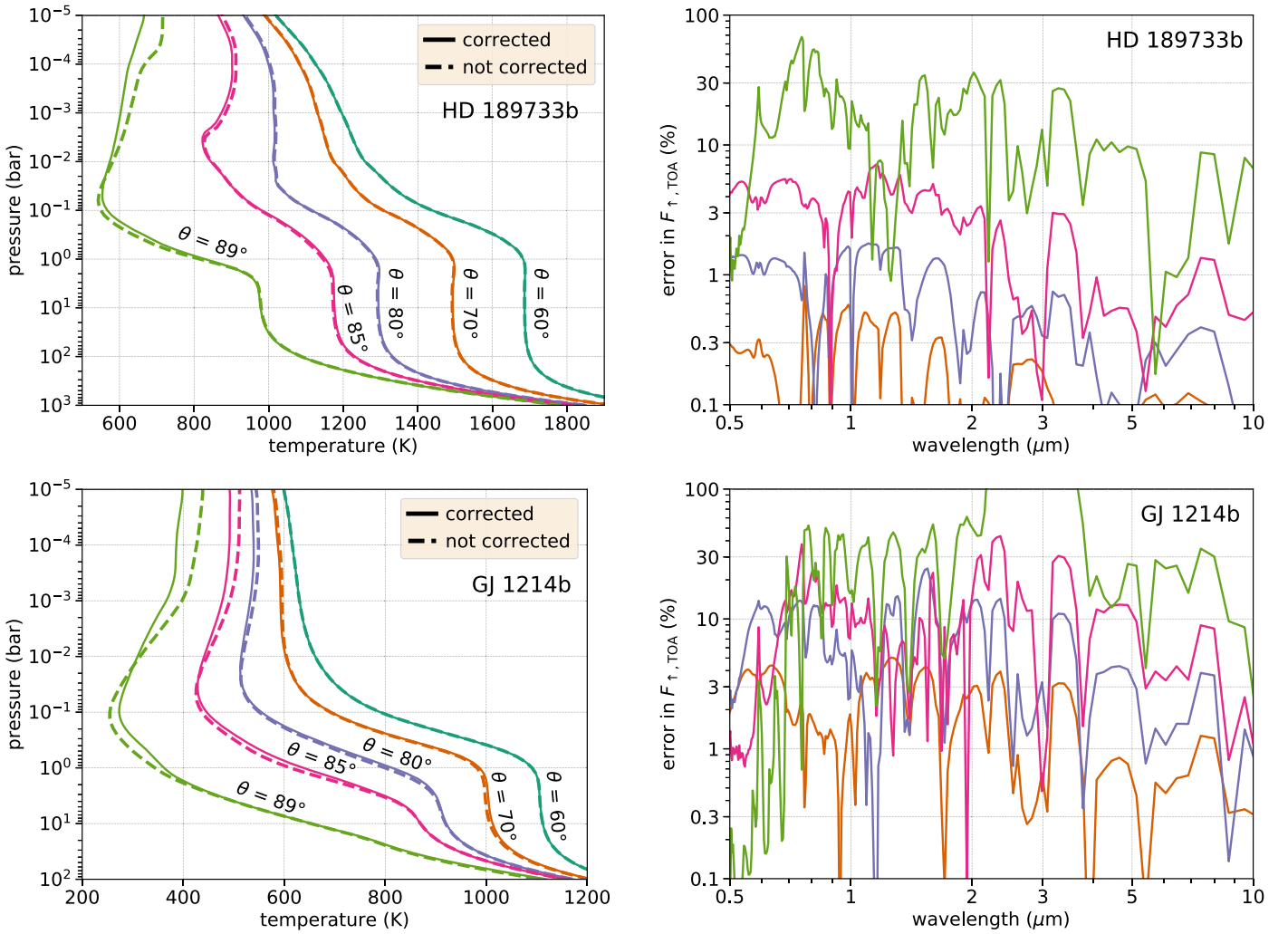


Figure 11. Left panels: temperatures in radiative–convective equilibrium for models with and without the stellar path length correction. The effect of the correction is shown for various zenith angles θ between 60° and 89° . Right panels: error in the outgoing top-of-atmosphere flux vs. wavelength when using the uncorrected model. The color-coding matches in the left and right panels. The $\theta = 60^\circ$ case is not shown, as the resulting error is smaller than the depicted values. The top row shows the results for HD 189733b, and the bottom row shows GJ 1214b (hydrogen-dominated atmosphere). Due to the strong flux dependence on the temperature T , a small relative error e in T translates roughly to the error $4e$ in the emitted flux.

Figure 10, the photospheres of HD 189733b and GJ 1214b are shown at the wavelength of the respective star’s peak emission. At these depths, the ratio of fluxes for HD 189733b and GJ 1214b is ~ 2 and ~ 3 for zenith angles of 80° and ~ 1.1 and ~ 1.3 for zenith angles of 70° , respectively. We find the effect of the path length correction to be larger for GJ 1214b than for HD 189733b. This is because the path length error, when ignoring the correct geometry, scales with the relative width of the atmosphere, which is given by the ratio of the atmospheric scale height over the planetary radius H/R_{pl} . This ratio is larger for GJ 1214b, assuming a hydrogen-dominated atmosphere, than it is for HD 189733b. In fact, we estimate that $(H/R_{\text{pl}})_{\text{GJ}1214b} \sim 0.02$, whereas $(H/R_{\text{pl}})_{\text{HD}189733b} \sim 0.003$. For comparison, the Earth exhibits $(H/R_{\text{pl}})_{\text{Earth}} \sim 0.001$, meaning that the Earth’s atmosphere is geometrically thinner compared to higher-mass planets.

As a second test we run the fully self-consistent simulation with and without path length correction. We find that the impact of the correction on the temperature profile is negligible for zenith angles up to 70° ; see Figure 11 (left panels). For zenith angles $\theta > 80^\circ$, the effect becomes noticeable, with the

uncorrected models overestimating the upper atmospheric heating (pressure $\lesssim 0.1$ bar). Consequently, due to the larger attenuation of the stellar flux above, the lower atmospheric layers (pressure $\gtrsim 0.1$ bar) are cooler in the uncorrected models. As in the previous test, the effect is significantly larger for GJ 1214b than for HD 189733b. In Figure 11 (right panels), we show the effect of the path length correction on the resulting emission spectra. Depicted is the wavelength-dependent percentage error in the outgoing TOA flux of the uncorrected versus the corrected model for different zenith angles, color-coded analogously to the left panels. For HD 189733b, the errors in the spectrum are exceeding the percent level for zenith angles higher than 80° . For GJ 1214b, even $\theta = 70^\circ$ leads to errors of several percent for some wavelengths. For both planets, very close at the planetary limb ($\theta = 89^\circ$), the error in the flux is close to or exceeds 100%. It may be surprising that even though the temperatures in the different models are very similar, the error in the flux is significant for high zenith angles. Since the emitted flux depends on the temperature as T^4 , a small relative error in T translates to roughly four times the error in the flux.

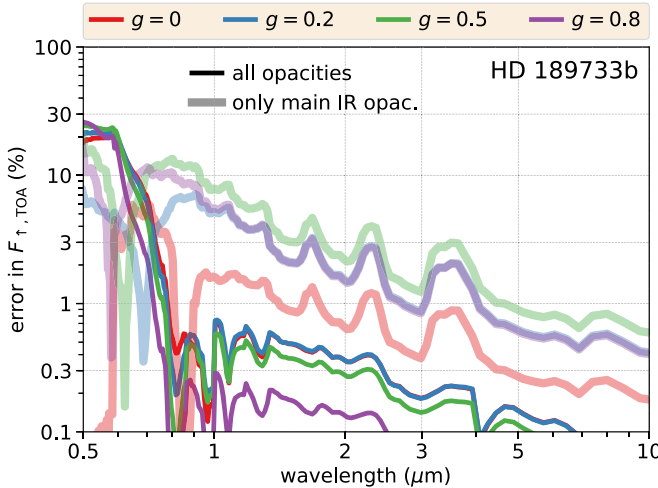


Figure 12. Error in the outgoing top-of-atmosphere flux in the hemispheric two-stream model compared to a model that includes the scattering correction. The fluxes are modeled self-consistently for the dayside of HD 189733b. Two tests are conducted, one with all opacity sources (see Table 1) and one with only the main infrared absorbers (Figure 3, top right panel).

Based on these tests, we conclude that in most cases, the path length correction should play a secondary role for zenith angles up to around 70° . However, if investigating planetary limb regions with zenith angles around 80° or higher, we recommend using the path length correction for the accuracy of both the modeled temperatures and the spectra. If the atmosphere is expected to be very extended, it may be reasonable to include the correction for zenith angles from 70° upward.

4.5. Impact of the Scattering Correction

We explore the effects of the scattering correction, which we have implemented into the hemispheric two-stream formalism of HELIOS (see Section 2.5). We self-consistently calculate the dayside temperatures and the corresponding spectral emission of HD 189733b, once with and once without the scattering correction. As we do not include clouds in this work, the only present scattering originates from hydrogen Rayleigh scattering. In this case, we would expect isotropic scattering, where $g_0 = 0$. However, to increase the tested parameter range, we artificially vary g_0 between 0 and 1 to account for different kinds of scattering particles. The value of ω_0 is given by

$$\omega_0 = \frac{\sigma_{\text{H},\text{H}_2}}{\sigma_{\text{H},\text{H}_2} + \sigma_{\text{mol}}}, \quad (29)$$

where $\sigma_{\text{H},\text{H}_2}$ is the Rayleigh scattering cross section due to H and H_2 , and σ_{mol} is the cross section due to molecular absorption.

In the first test, we use our full opacity list and find that the atmospheric temperatures do not change noticeably. Including the scattering correction, the deeper layers (pressure < 1 bar) merely warm about 1–2 K compared to the nominal case, regardless of the used g_0 (not shown). However, turning our attention to the TOA emitted flux, we find that the correction decreases the backscattered light in the optical wavelengths by about 10%–30%; see Figure 12. For longer wavelengths, the discrepancy drops below 1%, as here the outgoing flux is dominated by thermal emission. In general, we also observe that the discrepancy, i.e., the error in the uncorrected model,

becomes smaller as g_0 approaches unity. This may appear counterintuitive, as one could think that two-stream methods fare more poorly for larger aerosols, which exhibit forward scattering ($g_0 \approx 1$). However, our results are consistent with those of Heng et al. (2018), well visualized in their Figure 1, who showed that the scattering correction vanishes, i.e., the factor $E \rightarrow 1$, as g_0 goes to unity. Apart from this, we find our reduction of scattered flux consistent with Kitzmann et al.’s (2013) result that two-stream methods overpredict scattering by up to 20%.

In a second test, we include only the main infrared absorbers, shown in Figure 3 (top right panel). In this way, it is the Rayleigh scattering that becomes responsible for the bulk of the stellar flux extinction. This significantly increases the value of w_0 in the optical wavelengths (see Equation (29)), making the impact of the scattering correction larger. In this scenario, the bottom atmospheric temperatures diverge between 50 and 200 K depending on the g_0 parameter, and the corrected model is again warmer in the bottom (not shown). Hence, tuning the strength of the scattering directly affects the extent of the greenhouse warming. The thermal emission is subsequently more discrepant, caused by the larger temperature differences between the models. As can be seen in Figure 12, the error exceeds several percent in the near-infrared. The scattered flux discrepancy in the optical is with values around 10% on the same order of magnitude as in the previous test.

We conclude that the scattering correction provides a significant improvement for the accuracy of the stellar flux scattering. If scattering dominates over the absorption at shorter wavelengths, any potential errors on the stellar flux propagate to the temperatures and thermal emission.

4.6. Atmospheric Model Library

In addition to the model comparisons and numerical tests presented, we also include self-consistently calculated cloud-free atmospheric models using our improved radiative transfer code HELIOS. We include the full opacity list, as given in Table 1, and the scattering correction, as described in Section 2.5. Each model output provides, among others, the atmospheric temperature profile in radiative–convective equilibrium and a post-processed high-resolution emission spectrum, as described in Section 3.2. Additionally, it contains information about any other calculated quantity, like the entropy, optical depth, contribution function, etc.

Below, we first describe the parameters of the grid for the self-luminous planets, and then we elaborate on the calculated sample of irradiated planets. Finally, we provide information on how to download the models.

4.6.1. Grid of Self-luminous Planets

The calculated atmosphere grids for self-luminous planets span the following dimensions. The effective temperature range is $T_{\text{eff}} = [200, 3000]$ K with a step size $\Delta T_{\text{eff}} = 100$ K. The surface gravity, $\log_{10} g = [1.4, 5.0]$, with $\Delta \log_{10} g = 0.2$, $[g] = \text{cm s}^{-2}$. The metallicity range is $[M/\text{H}] = [-1, 1]$ with $\Delta[M/\text{H}] = 0.5$, where we write

$$\left[\frac{M}{\text{H}} \right] = \log_{10} \left(\frac{n_M}{n_{\text{H}}} \right) - \log_{10} \left(\frac{n_{M,\odot}}{n_{\text{H},\odot}} \right), \quad (30)$$

with n_X being the number density of element X and $n_{X,\odot}$ being the solar photospheric value (Asplund et al. 2009). We write M

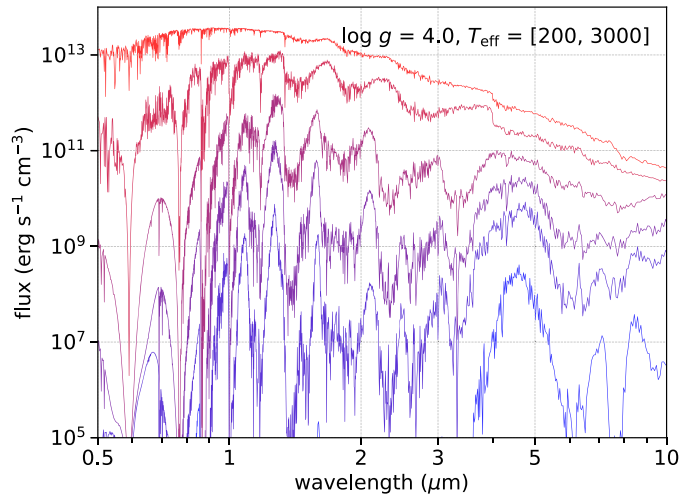
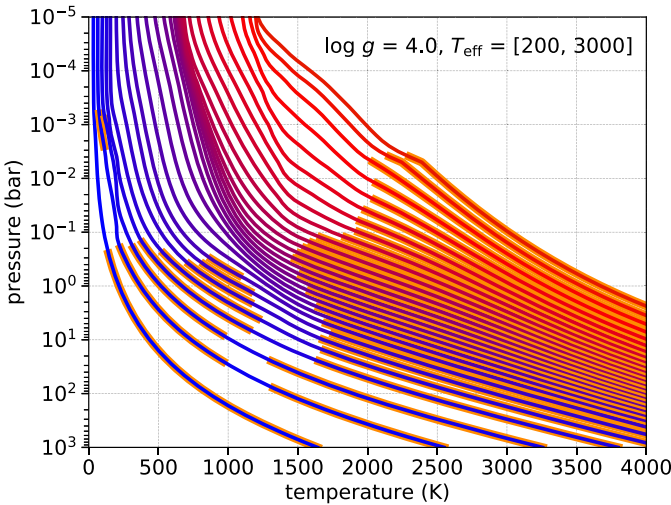


Figure 13. Left: grid of temperatures in radiative–convective equilibrium for various effective temperatures ($\Delta T_{\text{eff}} = 100$ K) using $\log_{10} g = 4.0$. Convective zones are marked with wider orange lines. Right: top-of-atmosphere emission spectra for a subset of the calculated models. Depicted are six models with $T_{\text{eff}} = 200, 400, 600, 1000, 2000$, and 3000 K using solar metallicity and C/O ratio. The spectra are downsampled in resolution for clarity.

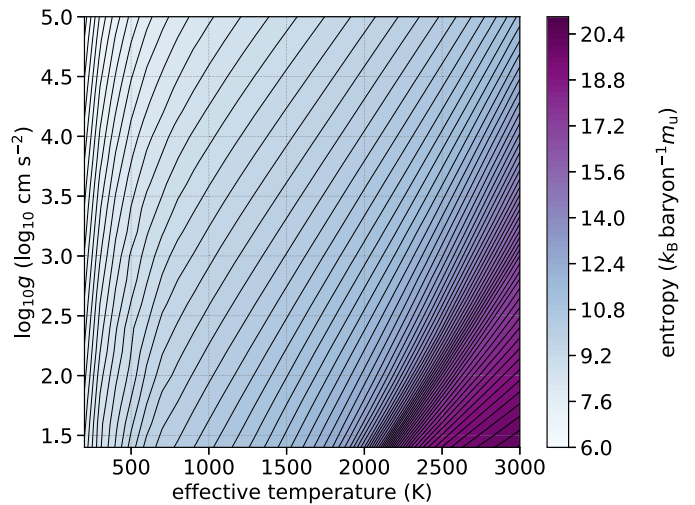
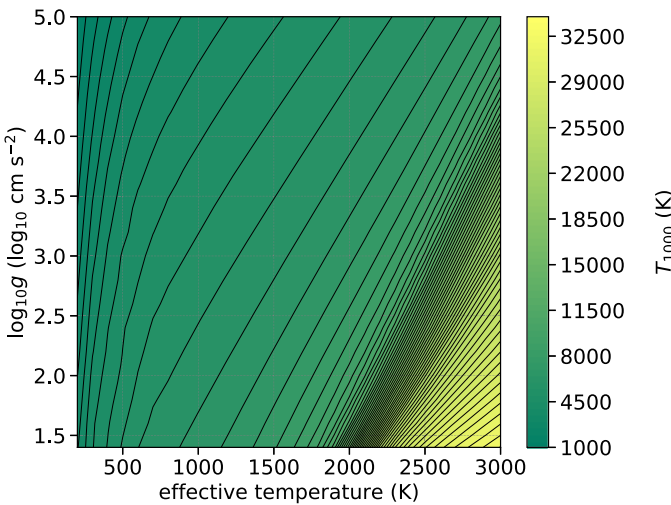


Figure 14. Temperature in the deep convective zone at a pressure of 1000 bars, T_{1000} (left), and the entropy (right) for the model grid calculated, spanning a range in effective temperature and surface gravity g . The contour lines are separated by 500 K on the left and $0.2 k_{\text{B}}$ baryon $^{-1} m_{\text{u}}$ on the right, with k_{B} being the Boltzmann constant and m_{u} the atomic mass unit. Depicted are the models for solar metallicity and C/O ratio.

for every element heavier than helium. For each metallicity, we further calculate models with three values for the C/O ratio: 0.1, solar (0.55), and 1. The temperatures are calculated until a pressure of 1000 bars, so that every model atmosphere couples to the deep convective zone. The limits of the grid are chosen to accommodate low-mass young planets and brown dwarfs and will be extended in future to include older, high-mass brown dwarfs with $\log_{10} g > 5$.

Figure 13 shows an excerpt of the grid for self-luminous planets for various effective temperatures using $\log_{10} g = 4.0$. Displayed are the temperatures in radiative–convective equilibrium and the corresponding TOA emission spectra for some of the models. Note that the spectra shown are downsampled from the native resolution for clarity.

Figure 14 (left panel) shows the temperature at a pressure of 1000 bars, T_{1000} , for the model grid calculated. As T_{1000} lies within the deep convective zone for all calculated models, it can be used directly to extrapolate to the interior adiabat (see

Burrows et al. 1997). Otherwise, we also provide the entropy for direct coupling; see Figure 14 (right panel).

In addition to the spectral fluxes, we provide a table with the expected magnitudes at the planetary surface for the NACO J , H , K_s , and L' filter bandpasses; see Figure 15 for an excerpt. They are calculated by convolving the filter profiles with the spectral flux. With a Vega spectrum,¹³ the zero-points were obtained. For more details, see Linder et al. (2019).

4.6.2. Sample of Irradiated Planets

In addition to the self-luminous planets, we provide atmospheric models for a sample of irradiated planets of interest. Table 2 lists the planets currently included in our model library, together with the system parameters used. For each planet, we calculate $3 \times 3 \times 2 = 18$ models, where we vary the metallicity, $[M/\text{H}] = -1, 0, 1$, C/O = 0.1, solar (0.55), 1,

¹³ From the *Hubble Space Telescope* Science Institute website as alpha_lyr_stis_003.txt.

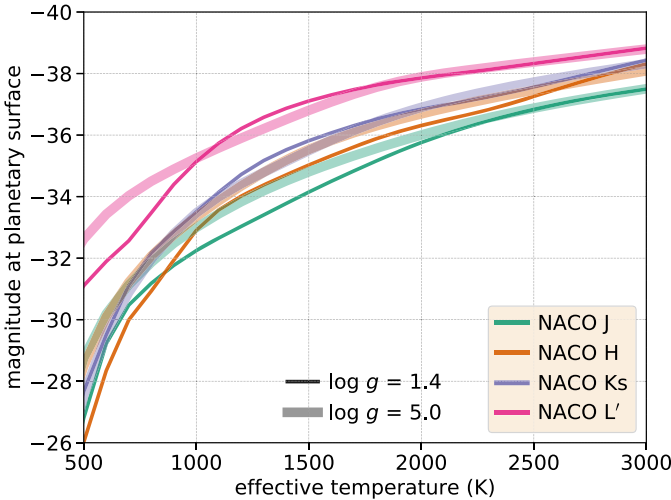


Figure 15. Left: magnitude at the planetary surface for the NACO J , H , Ks , and L' filters for self-luminous planets of varying effective temperature, shown for two surface gravities. Right: self-luminous planets of varying effective temperature vs. NACO $J-Ks$ magnitude. The surface gravities shown range from $\log_{10} g = 1.4$ (blue) to $\log_{10} g = 5.0$ (green). Depicted are the models for solar metallicity and C/O ratio.

Table 2
System Parameters Used in This Study

Name	R_{pl}	$\log_{10} g$	a	R_*	T_*
GJ 1132b ^a	0.1058	3.068	0.0153	0.207	3270
GJ 436b ^b	0.38	3.106	0.04085	0.464	3684
HD 189733b ^c	1.216	3.29	0.03142	0.805	5050
Kepler-7b ^d	1.614	2.62	0.06246	1.966	5933
KELT-9b ^e	1.891	3.30	0.03462	2.362	9560
WASP-8b ^f	1.038	3.74	0.0801	0.945	5600
WASP-12b ^g	1.776	3.066	0.02293	1.595	6300
WASP-14b ^h	1.281	4.01	0.036	1.306	6475
WASP-18b ⁱ	1.165	4.281	0.0247	1.23	6400
WASP-19b ^j	1.386	3.143	0.01655	0.99	5500
WASP-33b ^k	1.679	3.46	0.0259	1.509	7430
WASP-43b ^l	1.036	3.672	0.0152	0.667	4520

Notes. R_{pl} (R_{Jup}): planetary radius; g (cm s^{-2}): surface gravity; a (au): orbital distance; R_* (R_\odot): stellar radius; T_* (K): stellar temperature.

^a Berta-Thompson et al. (2015); Southworth et al. (2017); Bonfils et al. (2018).

^b Butler et al. (2004).

^c Southworth (2010); de Kok et al. (2013); Boyajian et al. (2015).

^d Latham et al. (2010); Demory et al. (2011).

^e Gaudi et al. (2017).

^f Queloz et al. (2010).

^g Hebb et al. (2009); Chan et al. (2011).

^h Joshi et al. (2009).

ⁱ Southworth et al. (2009); Hellier et al. (2009).

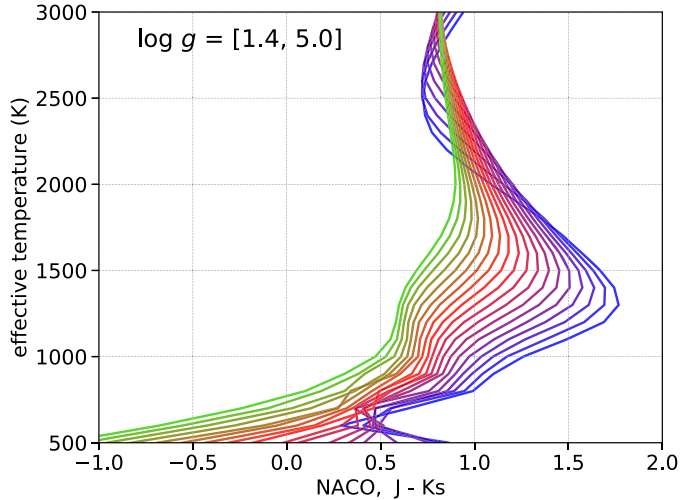
^j Hebb et al. (2010); Hellier et al. (2011).

^k Collier Cameron et al. (2010); Kovács et al. (2013); Lehmann et al. (2015).

^l Gillon et al. (2012).

and the heat redistribution factor $f = 1/2$, $2/3$. The latter parameter accounts for the heat redistribution efficiency from the dayside to the nightside (Burrows et al. 2008; Spiegel & Burrows 2010). Choosing $f = 1/2$ is computationally equivalent to setting the zenith angle to 60° . For these models, we conservatively use a blackbody for the stellar emission and an internal flux consistent with 75 K thermal emission.

Figure 16 displays the dayside temperatures and secondary eclipse spectra of the calculated planets for $f = 1/2$, solar metallicity, and three different C/O ratios. The planets are listed with increasing effective temperature.



4.6.3. Download

The atmospheric models are available for download on our server. For each model, we provide both the raw HELIOS output files and the temperature profile and emission spectrum alone. This gives both full access to all of the employed model parameters and quick access to the impatient.

The download link is given in the `readme` file of HELIOS in the GitHub repository <https://github.com/exoclime/HELIOS>.

Additionally, the same `readme` file describes the format of the output files and the directory structure.

The provided atmospheric models are a snapshot of current efforts. We plan to update them in regular intervals, e.g., when we incorporate new opacity data into our code. We also plan to extend the self-luminous planet grids to larger parameter ranges or, if requested, fill out the calculated grids by choosing smaller parameter steps. For the irradiated planets, we are going to include more objects as interest arises. Requests may be submitted to this work's lead author.

Finally, as all of our modeling tools used in this work, namely, HELIOS (Malik et al. 2017; this work), HELIOS-K (Grimm & Heng 2015), and FastChem (Stock et al. 2018), are open-source and publicly available at github.com/exoclime, the scientific community is encouraged to reproduce and test the model atmospheres provided.

5. Summary and Outlook

We have presented a number of methodological improvements and new ingredients to the radiative transfer code HELIOS. We have included must-have utilities that any radiative transfer package should contain and were dearly missing in the original version of HELIOS when it was introduced in Malik et al. (2017): the calculation of a direct irradiation beam, the possibility of convective adjustment, and the output of the contribution function. Additionally, we have vastly extended our list of opacity sources by including important metal oxides and hydrides, such as TiO, VO, AlO, SiH, the alkali metals, Na and K, and H^- , which play an imperative role for very hot atmospheres (Sharp & Burrows 2007). Furthermore, we have implemented a geometrical

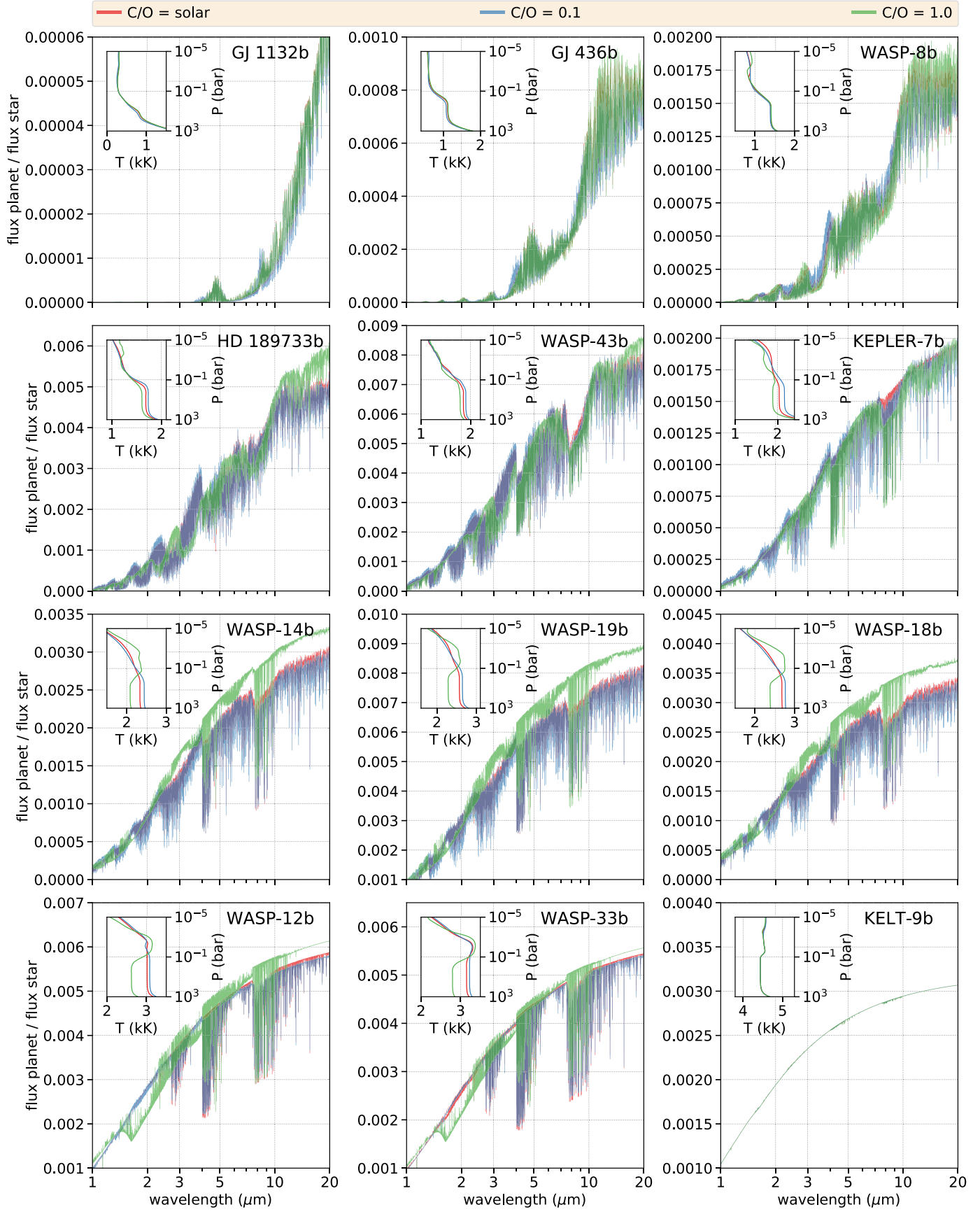


Figure 16. Secondary eclipse spectra and dayside temperature profiles for a varying C/O ratio and solar metallicity, shown for the sample of irradiated planets provided. The planets are listed with increasing effective temperature.

adjustment to the stellar path length and a scattering correction factor, new features that bring HELIOS on par with other state-of-the-art radiative transfer solvers for exoplanetary atmospheres on the market.

As part of this study, we have compared HELIOS with other radiative transfer codes and found good consistency with their results, given the diversity of radiative transfer techniques and differences in the opacities between the models. Also, we have checked the impact of different sets of opacities and new incorporated additions to the code on atmospheric properties. We have found that with higher atmospheric temperatures, it becomes increasingly important to employ metal hydrides, metal oxides, and H⁻ opacities, as their abundance and thus influence on atmospheric extinction grows. We have found that the solar path length correction leads to significant improvements for zenith angles over 80°, or even 70° for widely extended atmospheres. Finally, the scattering correction improves the accuracy of stellar light scattering compared to the hemispheric two-stream method by 10%–30%, which is consistent with what earlier studies found (Kitzmann et al. 2013).

With HELIOS, we have generated a large grid of self-consistently calculated model atmospheres for self-luminous planets and brown dwarfs. The goal is to provide the community with atmospheres that can be used by planetary evolution models as constraints on the cooling rate of evolving planets. The corresponding high-resolution spectra help assess the planet’s observability during the planet’s evolution. We hereby follow up on previous efforts (e.g., Burrows et al. 1997; Spiegel & Burrows 2012).

We have further calculated dayside atmospheres for a sample of irradiated planets of interest, which may be used for spectral reconnaissance and to study the influence of various chemical compositions on the dayside temperatures and spectral signatures. In particular, very hot and ultrahot Jupiters like WASP-103b, WASP-33b, KELT-20b, and particularly KELT-9b pique current interests, as, with dayside temperatures exceeding 3000 K, they are expected to offer a view into their atmospheric structure without obstruction by thermodynamically formed and chemical disequilibrium clouds. Self-consistent models, such as HELIOS, may provide useful constraints on the feasibility of atmospheric characterizations with current and future telescopes like the *Hubble* and *James Webb Space Telescopes*.

For the future, we see many opportunities for how to expand on the current work. We plan to self-consistently include disequilibrium chemistry, which is important for correct estimates of the strength of spectral features (Drummond et al. 2016). Furthermore, for colder planets, clouds are likely to present a significant hindrance, since their strong scattering and absorption may substantially mask spectral signatures. Although we currently do not include clouds in our calculations, we are able to predict if an observed atmosphere is consistent with a cloud-free scenario. We may tackle the cloud question in a future study. A cloud scheme sufficient to assess the spectroscopic impact of aerosols could consist of the following components: a cloud structure model (Ackerman & Marley 2001; Gao & Benneke 2018; Ohno & Okuzumi 2018), an estimate of the condensate species and grain composition (Lee et al. 2018), and corresponding extinction efficiencies (Kitzmann & Heng 2018).

M.M., D.K., J.M., S.G., G.-D.M., E.L., S.-M.T., and K.H. thank the Swiss National Science Foundation (SNF), the Center for Space and Habitability (CSH), the PlanetS National Center of Competence in Research (NCCR), and the MERAC Foundation for partial financial support. G.-D.M. acknowledges the support of the DFG priority program SPP 1992 “Exploring the Diversity of Extrasolar Planets” (KU 2849/7-1) and the Swiss National Science Foundation under grant BSSGI0_155816 “PlanetsInTime.” Furthermore, the authors thank P. Cubillos for sharing his recipe for the alkali resonance wings and S. Gandhi for sharing his model data. Lastly, we thank the anonymous referee for improving the quality of this work.

This work has made use of the VALD database, operated at Uppsala University, the Institute of Astronomy RAS in Moscow, and the University of Vienna.

Software: HELIOS (Malik et al. 2017; github.com/exoclime/helios), HELIOS-K (Grimm & Heng 2015; github.com/exoclime/helios-k), FastChem (Stock et al. 2018; github.com/exoclime/fastchem), CUDA (Nickolls et al. 2008), PyCUDA (Klöckner et al. 2012), python (van Rossum 1995), scipy (Oliphant 2007), numpy (van der Walt et al. 2011), matplotlib (Hunter 2007).

Appendix A Calculation of the Alkali Opacities

We split the spectral lines of Na and K into two groups: the first consists of the four resonance lines, and the second contains all of the other, weaker lines. The lines in the two groups are calculated differently.

A.1. Resonance Lines

The four resonance lines alone, i.e., the D doublet for Na at 0.589 μm and the doublet for K I at 0.77 μm, account for very strong absorption in the optical and are among the most detectable spectral lines in exoplanets and brown dwarfs (Seager & Sasselov 2000; Burrows et al. 2002a; Charbonneau et al. 2002). For modeling purposes, they pose a substantial challenge, as their line wings deviate significantly from a Lorentzian profile. Attempts to characterize the resonance line wings are motivated by theoretical quantum chemistry and enhanced with laboratory measurements (Burrows et al. 2000; Burrows & Volobuyev 2003; Allard et al. 2012b, 2016). We model the far wings as a composite of the Voigt profile in the line core, stitched together with a damping prescription for the far wings as described in Burrows et al. (2000).

While we are aware of an ongoing debate between Burrows et al. and Allard et al. regarding the correct shape of the sodium and potassium profiles in the line wings, we have chosen to adopt the Burrows et al. (2000) and Burrows & Volobuyev (2003) formulation, as it is available in analytical form and straightforwardly implementable. Since the current study is focused on the methodology of HELIOS, rather than the interpretation of measured spectra, we deem it reasonable to defer this issue to a future study.

The line profiles in their core follow a Voigt profile with the collisional broadening half-widths at half-maximum (HWHMs) Γ calculated from impact theory. The used values are $\Gamma_{\text{Na}} = 0.071(T/2000 \text{ K})^{-0.7} \text{ cm}^{-1} \text{ atm}^{-1}$ for sodium and $\Gamma_{\text{K}} = 0.14(T/2000 \text{ K})^{-0.7} \text{ cm}^{-1} \text{ atm}^{-1}$ for potassium. Using statistical theory, the outer line wings are modeled by a power

law truncated with an exponential Boltzmann factor. The transition between those two regimes, called the location of detuning, happens at the frequency shift $\delta\nu$ from the line center. For sodium, we use $\delta\nu_{\text{Na}} = 30(T/500 \text{ K})^{0.6} \text{ cm}^{-1}$, and for potassium, we use $\delta\nu_{\text{K}} = 20(T/500 \text{ K})^{0.6} \text{ cm}^{-1}$, where T is the temperature (Unsold 1955; Nefedov et al. 1999; Burrows et al. 2000; Iro et al. 2005). The total line profile at frequency ν is given by

$$\Phi(\nu) = \begin{cases} \Phi_V(\nu - \nu_0) & \text{if } |\nu - \nu_0| \leq \delta\nu, \\ \Phi_V(\nu) \left(\frac{\delta\nu}{\nu - \nu_0} \right)^{3/2} \exp \left[-\frac{h(\nu - \nu_0)}{k_B T} \right] & \nu_0 > \delta\nu, \end{cases} \quad (31)$$

where Φ_V is the Voigt profile, ν_0 is the line center frequency, $\delta\nu$ is the distance from the detuning points to the line center, and h and k_B are the Planck and Boltzmann constants, respectively.

A.2. Other Lines

The individual impact of the weaker lines is smaller, and their far wings play a subdominant role. Hence, they are sufficiently modeled with a classical Voigt profile.

In the following, we briefly outline the expressions and parameters used in our nominal method to calculate atomic lines. The frequency ν dependent cross section is given by $\sigma_\nu = S \cdot \Phi_\nu$, where the line strength S and the profile Φ_ν are calculated independently. The line strength can be expressed as

$$S = \frac{\pi e^2 g_i f_{ij}}{m_e c} \frac{e^{-E_i/k_B T}}{Q(T)} (1 - e^{-\Delta E/k_B T}), \quad (32)$$

where i and j denote the lower and upper quantum states, e is the electron charge, g is the statistical weight, f is the oscillator strength, m_e is the electron mass, c is the speed of light, E is the energy, Q is the partition function, and the energy difference $\Delta E = E_j - E_i$. Also, $\Delta E = h\nu$, with ν being the frequency of the absorbed or emitted photon.

The partition function is defined as

$$Q(T) = \sum_k q_k e^{-E_k/k_B T}, \quad (33)$$

where the sum leads over all allowed quantum states k . It can be either calculated directly from the energy levels, approximated by fitting functions, or read from precalculated tables.

As the ExoMol or HITRAN databases do not feature atomic species, we have taken the necessary spectral data from the Kurucz line list.¹⁴ With g_i , f_{ij} , E_i , and E_j provided in the database, the line strength is fully determined. Note that it is common to tabulate $\log_{10}(g_i f_{ij})$ instead of the individual g_i and f_{ij} quantities.

The Voigt profile Φ_V at frequency ν is defined as the convolution between the Doppler Φ_D and Lorentz profiles Φ_L . Through

$$\Phi_V(\nu; \Gamma_D, \Gamma_L) = \int_{-\infty}^{\infty} \Phi_L(\nu - \nu'; \Gamma_L) \Phi_D(\nu'; \Gamma_D) d\nu', \quad (34)$$

¹⁴ The Kurucz data are found at <http://kurucz.harvard.edu/>. We also recommend the NIST spectral database, which has a user-friendly online tool (https://physics.nist.gov/PhysRefData/ASD/lines_form.html).

the Voigt profile depends on the Doppler and Lorentz HWHMs Γ_D and Γ_L . For thermal velocities, the Doppler HWHM is given by

$$\Gamma_D = \frac{\nu}{c} \sqrt{\frac{2 \ln 2 k_B T}{m}}, \quad (35)$$

where m is the particle mass. The Lorentz HWHM is a combination of natural, collisional, Stark, and Van der Waals broadening, i.e., $\Gamma_L = \Gamma_{\text{nat}} + \Gamma_{\text{coll}} + \Gamma_{\text{Stark}} + \Gamma_{\text{VdW}}$. Natural broadening arises due to the limited lifetime of an excited quantum state and the subsequent uncertainty on the energy. Using the Kurucz database, we write

$$\Gamma_{\text{nat}} = \frac{10^{\Gamma_R}}{2\pi}, \quad (36)$$

where Γ_R is called the radiative damping coefficient and is a tabulated quantity. Collisional broadening is harder to quantify, as it depends on collisions with the surrounding gas and hence is a function of pressure and temperature. At the order-of-magnitude level, we estimate the HWHM due to collisions as (Heng et al. 2015)

$$\Gamma_{\text{coll}} = P \sigma_{\text{H}_2} \sqrt{\frac{2}{mk_B T}}, \quad (37)$$

where P is the pressure and $\sigma_{\text{H}_2} \sim 10^{-15} \text{ cm}^2$ is the cross section of molecular hydrogen, which we assume as the dominating collision partner. In this study, we neglect the remaining two broadening mechanisms due to Stark line splitting and Van der Waals perturbations. We refer to Sharp & Burrows (2007) for an excellent discussion of line profiles and the calculation of opacities.

On a final note, there is no closed analytical solution to calculate the Voigt integral (Equation (34)). However, the problem can be recast in the form of the real part of the complex Faddeeva function with sufficient accuracy (Zaghloul & Ali 2012). The Faddeeva function is included, e.g., in the `scipy` package for Python.

Appendix B Removal of Gas Species Due to Condensation

As described in Section 3.1, we employ a two-step determination of the chemical abundances for some major atmospheric species. There are two options. First, the gas species itself may condensate out. Hence, for each point in temperature T and pressure P , after the equilibrium abundance has been determined, we check whether it is located above or below the condensation curve for this species. If it is located below the curve, we remove it from our atmospheric catalog. Such a procedure is done for H_2O , TiO , and VO .

Apart from condensing out itself, the gas species may also participate in the formation of dust grains. If the species is the further limiting constituent in the grain formation process, it is expected to be removed from the gaseous phase. We apply an exponential decline starting at the dust grain condensation curve and then fit the gradient of the decline as shown in Sharp & Burrows (2007), which results in

$$f(T, P) = f_{\text{EQ}}(T_{\text{cond}}, P) \cdot 10^{-2.2(T_{\text{cond}} - T)}, \quad (38)$$

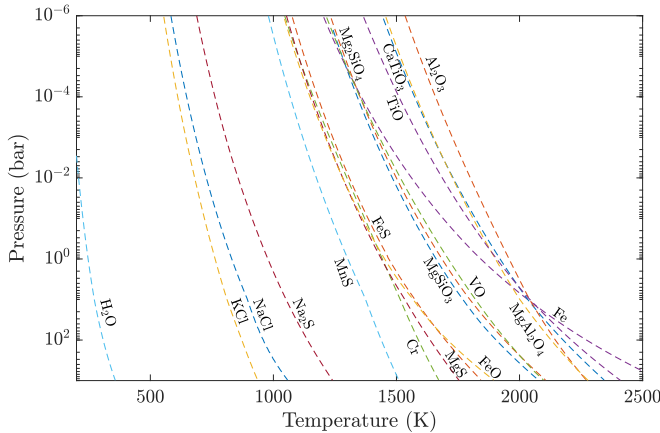


Figure 17. Sample of condensation curves for atmospheric gas species and dust grains. The shown curves assume solar elemental abundances and equilibrium chemistry.

where f is the volume mixing ratio, f_{EQ} is the one obtained from equilibrium chemistry, and T_{cond} is the condensation temperature at pressure P . We use this approach to remove the following gaseous species: SiO due to its participation in MgSiO_3 formation, Na for being in Na_2S , and K due to formation of KCl.

The calculation of the condensation curves themselves is based on the condensate data summarized in Woitke et al. (2018). We use FastChem to calculate the gas phase composition in chemical equilibrium for a grid of T - P points, assuming solar elemental abundances. As a second step, we then evaluate the potential condensation of various solid and liquid species. In cases where tabulated saturation vapor pressure data are available, we use these data to check if the partial pressure of a species in the gas phase exceeds its saturation vapor pressure at each T - P point. For other condensates, the Gibbs free energy of formation ΔG_f° is used to determine the potential presence. For a given condensate, e.g., $\text{A}_i\text{B}_j\text{C}_k$, we calculate the pseudo-activities a^c , given by

$$a^c = P_A^i P_B^j P_C^k e^{-\Delta G_f^\circ / RT}, \quad (39)$$

where P_A is the partial pressure of the condensate's constituent A in atomic form within the gas phase. A condensed species is stable if $a^c > 1$. At each T - P point, therefore, we check this condition to evaluate the potential presence of the corresponding solid or liquid. Note that the approach of using condensation curves treats each condensate individually and independently. In reality, different dust species compete for the various gas phase constituents, such that the resulting stable condensates might differ from the ones expected by the condensation curve approximation. An overview of how to treat a multicomponent gas–solid/liquid system in equilibrium can be found in Gail & Sedlmayr (2013).

A sample of condensation curves is shown in Figure 17. For completeness, we show not only the species used in this study but also other possible important condensates, which we plan to consider in future works.

Appendix C Smoothing of Temperatures

With the extension of the opacity list and the inclusion of strong shortwave absorbers like Na and K or TiO and VO, it is possible that discontinuities in the converged radiative equilibrium temperatures emerge. These discontinuities are not a mistake in the numerical code but an inherent flaw of a discrete one-dimensional grid treatment. Due to the interplay between chemical abundances and opacities and their intricate dependency on temperature and pressure, neighboring layers may be left with large differences in atmospheric abundances even after a converged radiative equilibrium solution has been found. This sometimes leads to jumps in the net flux and converged temperatures. However, we expect atmospheres to smooth out chemical abundances across adjacent layers due to small-scale dynamics. Hence, we include a smoothing term in our formalism to prevent unphysically large temperature jumps between neighboring grid cells.

For a given layer i , we write the arithmetic average of the temperatures of the adjacent layers, $T_{\text{average},i}$, as

$$T_{\text{average},i} = \frac{T_{i-1} + T_{i+1}}{2}. \quad (40)$$

In order to keep the temperature in layer i , T_i , reasonably close to this average, we set the smoothing term $\mathcal{F}_{\text{smooth},i}$ to

$$\mathcal{F}_{\text{smooth},i} = \alpha(T_{\text{average},i} - T_i)^\beta, \quad (41)$$

with the constant $\alpha = 1 \text{ erg s}^{-1} \text{ cm}^{-2} \text{ K}^{-\beta}$. The exponent β sets the strength of the smoothing. The difficulty is in finding a value of β so that the smoothing is effective but not strong enough to drive the temperatures too much out of radiative equilibrium. After some trial and error, we have found $\beta = 7$ to offer satisfactory behavior (not shown). Now the smoothing term is added to the regular net flux divergence term $\Delta \mathcal{F}_{i,-}$,

$$\Delta \mathcal{F}_{i,-}^{\text{new}} = \mathcal{F}_{\text{smooth},i} + \Delta \mathcal{F}_{i,-}, \quad (42)$$

forming the new smoothed flux divergence $\Delta \mathcal{F}_{i,-}^{\text{new}}$, which is used in

$$\Delta T_i = -\frac{1}{\rho_i c_{p,i}} \frac{\Delta \mathcal{F}_{i,-}^{\text{new}}}{\Delta z_i} \Delta t \quad (43)$$

to obtain the temperature step ΔT_i , where Δz_i is the layer height, ρ_i is the mass density, $c_{p,i}$ is the specific heat capacity, and Δt is the time step. How Equation (43) is used in the context of the temperature iteration is explained in detail in Malik et al. (2017).

Figure 18 shows the dayside temperature profile of WASP-12b in radiative–convective equilibrium with and without the smoothing term. The Na and K opacity absorbs a significant fraction of the stellar flux high up in the atmosphere and causes a discontinuity in the temperature profile. We find that the inclusion of the smoothing term has no impact on the emitted flux of the planet (not shown) because the discontinuity typically occurs in the optically thin region of the atmosphere.

Appendix D Global Energy Balance for the Convection Scheme

As pointed out in Section 2.2, global energy balance is not automatically achieved when using the vanilla convective adjustment scheme. In order to satisfy the global energy

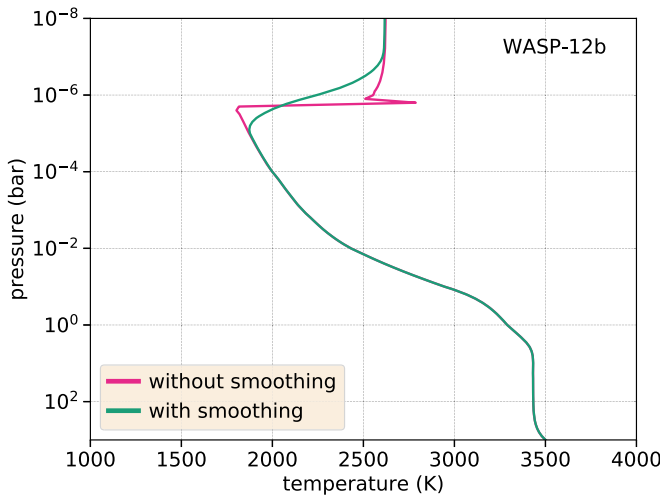


Figure 18. Dayside temperature profile of WASP-12b in radiative–convective equilibrium with and without the smoothing term. The Na and K opacity causes a discontinuity in the temperature profile high up in the atmosphere by absorbing a significant fraction of the incoming stellar radiation.

balance, the radiative net flux is required to be the same at the bottom of the atmosphere (BOA) and TOA. However, due to the convective zones, the radiative layers in the upper atmosphere do not “feel” the interior heat flux directly. Although they perfectly adjust to the local radiative balance, it proves difficult to establish radiative balance globally. In other words, in theory, we demand that

$$\mathcal{F}_- = \mathcal{F}_{\text{conv},-} + \mathcal{F}_{\text{rad},-} = \text{const} \quad (44)$$

holds throughout the atmosphere, where \mathcal{F}_- is the net flux, $\mathcal{F}_{\text{conv},-}$ is the net convective flux, and $\mathcal{F}_{\text{rad},-}$ is the net radiative flux. However, as the radiative heating and cooling only react to $\mathcal{F}_{\text{rad},-}$ and miss the contribution of $\mathcal{F}_{\text{conv},-}$, they try to adjust \mathcal{F}_- to a too-low constant value. The result is that the model deceptively converges to a radiative–convective solution but wrongly exhibits a TOA net flux lower than the BOA net flux. This dilemma can be fixed by modifying the temperatures in the convective region as

$$T'(P) = \Theta \left(\frac{P_0}{P} \right)^{-\kappa} f, \quad (45)$$

which is Equation (20) rewritten with an additional factor f . This factor fine-tunes the temperatures up or down if $\mathcal{F}_-(\text{TOA})$ is too low or too high. For planets with a nonvanishing interior heat flux, f reads

$$f = \left[\frac{X \cdot \mathcal{F}_{\text{rad},-}(\text{BOA})}{(X - 1) \cdot \mathcal{F}_{\text{rad},-}(\text{BOA}) + \mathcal{F}_{\text{rad},-}(\text{TOA})} \right]^\gamma, \quad (46)$$

where γ and X are dimensionless numbers. Once global equilibrium is reached, i.e., $\mathcal{F}_{\text{rad},-}(\text{TOA}) = \mathcal{F}_{\text{rad},-}(\text{BOA})$, f goes to unity, and we recover the conventional Equation (20). The most straightforward version of Equation (46) comes with $X = 1$, but if at some point during the iteration $\mathcal{F}_{\text{rad},-}(\text{TOA}) < 0$ occurs, the expression breaks down. Hence, choosing $X \gg 1$ provides numerical stability. In terms of γ , we have found through tweaking that a value of $\sim 10^{-2}$ suffices to do the trick. When modeling planets with a vanishing interior heat flux, e.g., small rocky planets, Equation (46) is not

applicable, as it returns zero. In this case, we write f as

$$f = \left[\frac{\mathcal{F}_{\text{rad},\downarrow}(\text{TOA})}{\mathcal{F}_{\text{rad},\uparrow}(\text{TOA})} \right]^\gamma, \quad (47)$$

where $\mathcal{F}_{\text{rad},\downarrow}(\text{TOA})$ and $\mathcal{F}_{\text{rad},\uparrow}(\text{TOA})$ are the total downward and upward fluxes at the TOA.

Lastly, we assume global energy equilibrium if

$$\frac{|\mathcal{F}_{\text{rad},-}(\text{BOA}) - \mathcal{F}_{\text{rad},-}(\text{TOA})|}{\mathcal{F}_{\text{rad},-}(\text{BOA})} < \epsilon \quad (48)$$

in the case with $\mathcal{F}_{\text{rad},-}(\text{BOA}) \neq 0$ and if

$$\frac{|\mathcal{F}_{\text{rad},-}(\text{TOA})|}{\mathcal{F}_{\text{rad},\downarrow}(\text{TOA})} < \epsilon \quad (49)$$

in the case with $\mathcal{F}_{\text{rad},-}(\text{BOA}) = 0$. We use $\epsilon = 10^{-4}$ in this work.

Appendix E Expressing the Heat Capacity in Terms of the Adiabatic Coefficient

Here we proceed to express the constant-pressure heat capacity c_p in a form similar to Equation (2.11) of Pierrehumbert (2010), $c_p = k_B / (\mu m_u \kappa)$, but valid also at dissociation and ionization. Let us start with the usual expression,

$$c_p = T \left(\frac{\partial S}{\partial T} \right)_P. \quad (50)$$

By the triple-product rule,

$$\begin{aligned} \left(\frac{\partial S}{\partial T} \right)_P &= - \left(\frac{\partial P}{\partial T} \right)_S \left(\frac{\partial S}{\partial P} \right)_T \\ &= - \left(\frac{\partial \ln P}{\partial \ln T} \right)_S \frac{P}{T} \left(\frac{\partial S}{\partial P} \right)_T. \end{aligned} \quad (51)$$

The first factor in Equation (51) being nothing else than $1/\kappa$ by its definition (Equation (15)), inserting Equation (51) into Equation (50) leads to

$$c_p = \frac{1}{\kappa} \left(- \frac{\partial S}{\partial \ln P} \right)_T = \frac{k_B}{m_u \kappa} \left(- \frac{\partial \tilde{S}}{\partial \ln P} \right)_T, \quad (52)$$

where $\tilde{S} \equiv S / (k_B / m_u)$ is the specific entropy in natural (dimensionless) units. Equation (52) is the same as Equation (22).

ORCID iDs

- Matej Malik <https://orcid.org/0000-0002-2110-6694>
- Daniel Kitzmann <https://orcid.org/0000-0003-4269-3311>
- João M. Mendonça <https://orcid.org/0000-0002-6907-4476>
- Simon L. Grimm <https://orcid.org/0000-0002-0632-4407>
- Shang-Min Tsai <https://orcid.org/0000-0002-8163-4608>
- Kevin Heng <https://orcid.org/0000-0003-1907-5910>

References

- Ackerman, A. S., & Marley, M. S. 2001, *ApJ*, 556, 872
- Alibert, Y., Mordasini, C., Benz, W., & Winisdoerffer, C. 2005, *A&A*, 434, 343

- Allard, F. 2014, in IAU Symp. 299, Exploring the Formation and Evolution of Planetary Systems, ed. M. Booth, B. C. Matthews, & J. R. Graham (Cambridge: Cambridge Univ. Press), 271
- Allard, F., & Hauschildt, P. H. 1995, *ApJ*, 445, 433
- Allard, F., Hauschildt, P. H., Alexander, D. R., Tamanai, A., & Schweitzer, A. 2001, *ApJ*, 556, 357
- Allard, F., Homeier, D., & Freytag, B. 2011, in ASP Conf. Ser. 448, 16th Cambridge Workshop on Cool Stars, Stellar Systems, and the Sun, ed. C. Johns-Krull, M. K. Browning, & A. A. West (San Francisco, CA: ASP), 91
- Allard, F., Homeier, D., & Freytag, B. 2012a, *RSPTA*, 370, 2765
- Allard, N. F., Kielkopf, J. F., Spiegelman, F., Tinetti, G., & Beaulieu, J. P. 2012b, *A&A*, 543, A159
- Allard, N. F., Spiegelman, F., & Kielkopf, J. F. 2016, *A&A*, 589, A21
- Amundsen, D. S., Baraffe, I., Tremblin, P., et al. 2014, *A&A*, 564, A59
- Armstrong, B. 1968, *JQSRT*, 8, 1577
- Asplund, M., Grevesse, N., Sauval, A. J., & Scott, P. 2009, *ARA&A*, 47, 481
- Azzam, A. A. A., Tennyson, J., Yurchenko, S. N., & Naumenko, O. V. 2016, *MNRAS*, 460, 4063
- Baraffe, I., Chabrier, G., & Barman, T. 2008, *A&A*, 482, 315
- Baraffe, I., Chabrier, G., Barman, T. S., Allard, F., & Hauschildt, P. H. 2003, *A&A*, 402, 701
- Barber, R. J., Tennyson, J., Harris, G. J., & Tolchenov, R. N. 2006, *MNRAS*, 368, 1087
- Barman, T. S., Hauschildt, P. H., & Allard, F. 2005, *ApJ*, 632, 1132
- Barton, E. J., Yurchenko, S. N., & Tennyson, J. 2013, *MNRAS*, 434, 1469
- Baudino, J.-L., Bézard, B., Boccaletti, A., et al. 2015, *A&A*, 582, A83
- Baudino, J.-L., Mollière, P., Venot, O., et al. 2017, *ApJ*, 850, 150
- Berta-Thompson, Z. K., Irwin, J., Charbonneau, D., et al. 2015, *Natur*, 527, 204
- Bonfils, X., Almenara, J.-M., Cloutier, R., et al. 2018, *A&A*, 618, A142
- Borysow, A. 2002, *A&A*, 390, 779
- Borysow, A., Jorgensen, U. G., & Fu, Y. 2001, *JQSRT*, 68, 235
- Boyajian, T., von Braun, K., Feiden, G. A., et al. 2015, *MNRAS*, 447, 846
- Burrows, A., Budaj, J., & Hubeny, I. 2008, *ApJ*, 678, 1436
- Burrows, A., Burgasser, A. J., Kirkpatrick, J. D., et al. 2002a, *ApJ*, 573, 394
- Burrows, A., Marley, M., Hubbard, W. B., et al. 1997, *ApJ*, 491, 856
- Burrows, A., Marley, M. S., & Sharp, C. M. 2000, *ApJ*, 531, 438
- Burrows, A., Ram, R. S., Bernath, P., Sharp, C. M., & Milsom, J. A. 2002b, *ApJ*, 577, 986
- Burrows, A., & Volobuyev, M. 2003, *ApJ*, 583, 985
- Butler, R. P., Vogt, S. S., Marcy, G. W., et al. 2004, *ApJ*, 617, 580
- Chabrier, G., Baraffe, I., Allard, F., & Hauschildt, P. 2000, *ApJ*, 542, 464
- Chan, T., Ingemyr, M., Winn, J. N., et al. 2011, *AJ*, 141, 179
- Chandrasekhar, S. 1960, Radiative Transfer (New York: Dover)
- Charbonneau, D., Brown, T. M., Noyes, R. W., & Gilliland, R. L. 2002, *ApJ*, 568, 377
- Collier Cameron, A., Guenther, E., Smalley, B., et al. 2010, *MNRAS*, 407, 507
- de Kok, R. J., Brogi, M., Snellen, I. A. G., et al. 2013, *A&A*, 554, A82
- Demory, B.-O., Seager, S., Madhusudhan, N., et al. 2011, *ApJL*, 735, L12
- Drummond, B., Tremblin, P., Baraffe, I., et al. 2016, *A&A*, 594, A69
- Fortney, J. J., Lodders, K., Marley, M. S., & Freedman, R. S. 2008, *ApJ*, 678, 1419
- Fortney, J. J., Marley, M. S., Lodders, K., Saumon, D., & Freedman, R. 2005, *ApJL*, 627, L69
- Gail, H.-P., & Sedlmayr, E. 2013, Physics and Chemistry of Circumstellar Dust Shells (Cambridge: Cambridge Univ. Press)
- Gandhi, S., & Madhusudhan, N. 2017, *MNRAS*, 472, 2334
- Gao, P., & Benneke, B. 2018, *ApJ*, 863, 165
- Gaudi, B. S., Stassun, K. G., Collins, K. A., et al. 2017, *Natur*, 546, 514
- Gillon, M., Triaud, A. H. M. J., Fortney, J. J., et al. 2012, *A&A*, 542, A4
- Goody, R. M., & Yung, Y. L. 1989, Atmospheric Radiation: Theoretical Basis (Oxford: Oxford Univ. Press)
- Gordon, I., Rothman, L., Hill, C., et al. 2017, *JQSRT*, 203, 3
- Grimm, S. L., & Heng, K. 2015, *ApJ*, 808, 182
- Hamre, B., Stammes, S., Stammes, K., & Stammes, J. J. 2013, in AIP Conf. Proc. 1531, Radiation Processes in the Atmosphere and Ocean, ed. R. F. Cahalan & J. Fischer (Melville, NY: AIP), 923
- Hansen, C. J., Kawaler, S. D., & Trimble, V. 2004, Stellar Interiors: Physical Principles, Structure, and Evolution (Berlin: Springer)
- Harris, G. J., Tennyson, J., Kaminsky, B. M., Pavlenko, Y. V., & Jones, H. R. A. 2006, *MNRAS*, 367, 400
- Hauschildt, P. H., & Baron, E. 1999, *JCoAM*, 109, 41
- Hebb, L., Collier-Cameron, A., Loeillet, B., et al. 2009, *ApJ*, 693, 1920
- Hebb, L., Collier-Cameron, A., Triaud, A. H. M. J., et al. 2010, *ApJ*, 708, 224
- Hellier, C., Anderson, D. R., Collier Cameron, A., et al. 2009, *Natur*, 460, 1098
- Hellier, C., Anderson, D. R., Collier-Cameron, A., et al. 2011, *ApJL*, 730, L31
- Helling, C., Dehn, M., Woitke, P., & Hauschildt, P. H. 2008, *ApJL*, 675, L105
- Heng, K., & Kitzmann, D. 2017, *MNRAS*, 470, 2972
- Heng, K., Malik, M., & Kitzmann, D. 2018, *ApJS*, 237, 29
- Heng, K., Mendonça, J. M., & Lee, J.-M. 2014, *ApJS*, 215, 4
- Heng, K., Wyttenbach, A., Lavie, B., et al. 2015, *ApJL*, 803, L9
- Hoeijmakers, H. J., Ehrenreich, D., Heng, K., et al. 2018, *Natur*, 560, 453
- Hubeny, I. 1988, *CoPhC*, 52, 103
- Hubeny, I., Burrows, A., & Sudarsky, D. 2003, *ApJ*, 594, 1011
- Hubeny, I., & Lanz, T. 1995, *ApJ*, 439, 875
- Hunter, J. D. 2007, *CSE*, 9, 90
- Husser, T.-O., Wende-von Berg, S., Dreizler, S., et al. 2013, *A&A*, 553, A6
- Iro, N., Bézard, B., & Guillot, T. 2005, *A&A*, 436, 719
- Irwin, P. G. J. 2009, Giant Planets of Our Solar System (Berlin: Springer)
- John, T. L. 1988, *A&A*, 193, 189
- Joseph, J. H., Wiscombe, W. J., & Weinman, J. A. 1976, *JAtS*, 33, 2452
- Joshi, Y. C., Pollacco, D., Collier Cameron, A., et al. 2009, *MNRAS*, 392, 1532
- Kitzmann, D. 2016, *ApJL*, 817, L18
- Kitzmann, D., & Heng, K. 2018, *MNRAS*, 475, 94
- Kitzmann, D., Heng, K., Rimmer, P. B., et al. 2018, *ApJ*, 863, 183
- Kitzmann, D., Patzer, A. B. C., & Rauer, H. 2013, *A&A*, 557, A6
- Klöckner, A., Pinto, N., Lee, Y., et al. 2012, *ParC*, 38, 157
- Kovács, G., Kovács, T., Hartman, J. D., et al. 2013, *A&A*, 553, A44
- Kreidberg, L., Line, M. R., Bean, J. L., et al. 2015, *ApJ*, 814, 66
- Kurucz, R. L. 1979, *ApJS*, 40, 1
- Kurucz, R. L. 2011, *CaPh*, 89, 417
- Latham, D. W., Borucki, W. J., Koch, D. G., et al. 2010, *ApJL*, 713, L140
- Lavie, B., Mendonça, J. M., Mordasini, C., et al. 2017, *AJ*, 154, 91
- Lee, G. K. H., Bleicic, J., & Helling, C. 2018, *A&A*, 614, A126
- Lee, H.-W., & Kim, H. I. 2004, *MNRAS*, 347, 802
- Lehmann, H., Guenther, E., Sebastian, D., et al. 2015, *A&A*, 578, L4
- Li, G., Gordon, I. E., Rothman, L. S., et al. 2015, *ApJS*, 216, 15
- Li, J., & Shibata, K. 2006, *JAtS*, 63, 1365
- Linder, E. F., Mordasini, C., Molliere, P., et al. 2019, *A&A*, 623, A85
- Line, M. R., Wolf, A. S., Zhang, X., et al. 2013, *ApJ*, 775, 137
- Lothringer, J. D., Barman, T., & Koskinen, T. 2018, *ApJ*, 866, 27
- Malik, M., Grosheintz, L., Mendonça, J. M., et al. 2017, *AJ*, 153, 56
- Manabe, S., Smagorinsky, J., & Strickler, R. F. 1965, *MWRv*, 93, 769
- Manabe, S., & Wetherald, R. T. 1967, *JAtS*, 24, 241
- Marleau, G.-D., & Cumming, A. 2014, *MNRAS*, 437, 1378
- Marley, M. S., & McKay, C. P. 1999, *Icar*, 138, 268
- Marley, M. S., Saumon, D., Guillot, T., et al. 1996, *Sci*, 272, 1919
- Márquez-Neila, P., Fisher, C., Sznitman, R., & Heng, K. 2018, *NatAs*, 2, 719
- McKay, C. P., Pollack, J. B., & Courtin, R. 1989, *Icar*, 80, 23
- McKemmish, L. K., Yurchenko, S. N., & Tennyson, J. 2016, *MNRAS*, 463, 771
- Meadows, V. S., & Crisp, D. 1996, *JGR*, 101, 4595
- Mendonça, J. M., Malik, M., Demory, B.-O., & Heng, K. 2018a, *AJ*, 155, 150
- Mendonça, J. M., Tsai, S.-M., Matej, M., Grimm, S. L., & Heng, K. 2018b, *ApJ*, 869, 107
- Mihalas, D. 1970, Stellar Atmospheres (San Francisco: Freeman)
- Mihalas, D. 1978, Stellar Atmospheres (2nd ed.; San Francisco: Freeman)
- Molliere, P., van Boekel, R., Bouwman, J., et al. 2017, *A&A*, 600, A10
- Molliere, P., van Boekel, R., Dullemond, C., Henning, T., & Mordasini, C. 2015, *ApJ*, 813, 47
- Mordasini, C., Alibert, Y., Georgy, C., et al. 2012, *A&A*, 547, A112
- Munari, U., Sordo, R., Castelli, F., & Zwitter, T. 2005, *A&A*, 442, 1127
- Murphy, T., & Meiksin, A. 2004, *MNRAS*, 351, 1430
- Nefedov, A. P., Sinel'shchikov, V. A., & Usachev, A. D. 1999, *PhyS*, 59, 432
- Nickolls, J., Buck, I., Garland, M., & Skadron, K. 2008, *Queue*, 6, 40
- Ohno, K., & Okuzumi, S. 2018, *ApJ*, 859, 34
- Oiphant, T. E. 2007, *CSE*, 9, 20
- Patrascu, A. T., Yurchenko, S. N., & Tennyson, J. 2015, *MNRAS*, 449, 3613
- Pierrehumbert, R. T. 2010, Principles of Planetary Climate (Cambridge: Cambridge Univ. Press)
- Prajpat, L., Jagoda, P., Lodi, L., et al. 2017, *MNRAS*, 472, 3648
- Queloz, D., Anderson, D. R., Collier Cameron, A., et al. 2010, *A&A*, 517, L1
- Richard, C., Gordon, I. E., Rothman, L. S., et al. 2012, *JQSRT*, 113, 1276
- Rivlin, T., Lodi, L., Yurchenko, S. N., Tennyson, J., & Le Roy, R. J. 2015, *MNRAS*, 451, 634
- Rothman, L. S., Gordon, I. E., Barber, R. J., et al. 2010, *JQSRT*, 111, 2139
- Ryabchikova, T., Piskunov, N., Kurucz, R. L., et al. 2015, *PhyS*, 90, 054005
- Saumon, D., Chabrier, G., & van Horn, H. M. 1995, *ApJS*, 99, 713
- Seager, S., & Sasselov, D. D. 2000, *ApJ*, 537, 916
- Sharp, C. M., & Burrows, A. 2007, *ApJS*, 168, 140

- Sneep, M., & Ubachs, W. 2005, *JQSRT*, **92**, 293
- Sousa-Silva, C., Al-Refaie, A. F., Tennyson, J., & Yurchenko, S. N. 2015, *MNRAS*, **446**, 2337
- Southworth, J. 2010, *MNRAS*, **408**, 1689
- Southworth, J., Hinse, T. C., Dominik, M., et al. 2009, *ApJ*, **707**, 167
- Southworth, J., Mancini, L., Madhusudhan, N., et al. 2017, *AJ*, **153**, 191
- Spiegel, D. S., & Burrows, A. 2010, *ApJ*, **722**, 871
- Spiegel, D. S., & Burrows, A. 2012, *ApJ*, **745**, 174
- Stamnes, K., Tsay, S.-C., Jayaweera, K., & Wiscombe, W. 1988, *ApOpt*, **27**, 2502
- Stock, J. W., Kitzmann, D., Patzer, A. B. C., & Sedlmayr, E. 2018, *MNRAS*, **479**, 865
- Sudarsky, D., Burrows, A., & Hubeny, I. 2003, *ApJ*, **588**, 1121
- Toon, O. B., McKay, C. P., Ackerman, T. P., & Santhanam, K. 1989, *JGR*, **94**, 16287
- Tsuji, T. 1967, in Colloq. on Late-Type Stars, ed. M. Hack (Trieste: Osservatorio Astronomico), 260
- Tsuji, T. 1978, *A&A*, **62**, 29
- Tsuji, T. 2002, *ApJ*, **575**, 264
- Underwood, D. S., Tennyson, J., Yurchenko, S. N., et al. 2016, *MNRAS*, **459**, 3890
- Unsold, A. 1955, Physik der Sternatmosphären: Mit Besonderer Berücksichtigung der Sonne (Berlin: Springer)
- van der Walt, S., Chris Colbert, S., & Varoquaux, G. 2011, *CSE*, **13**, 22
- van Rossum, G. 1995, Python Tutorial, Tech. Rep. CS-R9526
- Woitke, P., Helling, C., Hunter, G. H., et al. 2018, *A&A*, **614**, A1
- Wong, A., Yurchenko, S. N., Bernath, P., et al. 2017, *MNRAS*, **470**, 882
- Yadin, B., Veness, T., Conti, P., et al. 2012, *MNRAS*, **425**, 34
- Yurchenko, S. N., Barber, R. J., & Tennyson, J. 2011, *MNRAS*, **413**, 1828
- Yurchenko, S. N., Blisett, A., Asari, U., et al. 2016, *MNRAS*, **456**, 4524
- Yurchenko, S. N., & Tennyson, J. 2014, *MNRAS*, **440**, 1649
- Yurchenko, S. N., Williams, H., Leyland, P. C., Lodi, L., & Tennyson, J. 2018, *MNRAS*, **479**, 1401
- Zaghoul, M. R., & Ali, A. N. 2012, *ACM Trans. Math. Softw.*, **38**, 15